NASA/CR-2011-217158

The Fast Scattering Code (FSC): Validation Studies and Program Guidelines

Ana F. Tinetti and Mark H. Dunn
Mark H. Dunn, Consultants, Yorktown, Virginia

June 2011

NASA STI Program . . . in Profile

Since its founding, NASA has been dedicated to the advancement of aeronautics and space science. The NASA scientific and technical information (STI) program plays a key part in helping NASA maintain this important role.

The NASA STI program operates under the auspices of the Agency Chief Information Officer. It collects, organizes, provides for archiving, and disseminates NASA's STI. The NASA STI program provides access to the NASA Aeronautics and Space Database and its public interface, the NASA Technical Report Server, thus providing one of the largest collections of aeronautical and space science STI in the world. Results are published in both non-NASA channels and by NASA in the NASA STI Report Series, which includes the following report types:

- TECHNICAL PUBLICATION. Reports of completed research or a major significant phase of research that present the results of NASA programs and include extensive data or theoretical analysis. Includes compilations of significant scientific and technical data and information deemed to be of continuing reference value. NASA counterpart of peer-reviewed formal professional papers, but having less stringent limitations on manuscript length and extent of graphic presentations.

- TECHNICAL MEMORANDUM. Scientific and technical findings that are preliminary or of specialized interest, e.g., quick release reports, working papers, and bibliographies that contain minimal annotation. Does not contain extensive analysis.

- CONTRACTOR REPORT. Scientific and technical findings by NASA-sponsored contractors and grantees.

- CONFERENCE PUBLICATION. Collected papers from scientific and technical conferences, symposia, seminars, or other meetings sponsored or co-sponsored by NASA.

- SPECIAL PUBLICATION. Scientific, technical, or historical information from NASA programs, projects, and missions, often concerned with subjects having substantial public interest.

- TECHNICAL TRANSLATION. English-language translations of foreign scientific and technical material pertinent to NASA's mission.

Specialized services also include creating custom thesauri, building customized databases, and organizing and publishing research results.

For more information about the NASA STI program, see the following:

- Access the NASA STI program home page at *http://www.sti.nasa.gov*

- E-mail your question via the Internet to help@sti.nasa.gov

- Fax your question to the NASA STI Help Desk at 443-757-5803

- Phone the NASA STI Help Desk at 443-757-5802

- Write to:
  NASA STI Help Desk
  NASA Center for AeroSpace Information
  7115 Standard Drive
  Hanover, MD 21076-1320

NASA/CR-2011-217158

The Fast Scattering Code (FSC): Validation Studies and Program Guidelines

Ana F. Tinetti and Mark H. Dunn
Mark H. Dunn, Consultants, Yorktown, Virginia

National Aeronautics and
Space Administration

Langley Research Center
Hampton, Virginia 23681-2199

Prepared for Langley Research Center
under Contract NNL09AA17C

June 2011

Available from:

NASA Center for AeroSpace Information
7115 Standard Drive
Hanover, MD 21076-1320
443-757-5802

TABLE OF CONTENTS **Page**

1. INTRODUCTION

The Fast Scattering Code (FSC)[1,2] is a frequency domain noise prediction program developed at the NASA Langley Research Center (LaRC) to simulate the acoustic field produced by the interaction of known, time harmonic incident sound with bodies of arbitrary shape and surface impedance immersed in a potential flow. The code uses the equivalent source method (ESM) to solve an exterior 3-D Helmholtz boundary value problem (BVP) by expanding the scattered acoustic pressure field into a series of point sources (N_s) distributed on a fictitious surface placed inside the actual scatterer. The FSC discretizes the scattering surface into N_c collocation points to produce a dense, over-determined system of linear equations of size N_c x N_s; the unknown source strengths are adjusted so that a prescribed surface boundary condition is satisfied using least squares methods. The FSC has been validated using analytical[3,4] and experimental data[5,6], and applied successfully to various problems of interest to the aeroacoustics community[7-9].

The ESM is the most computationally efficient of the boundary methods currently used in acoustics (finite difference, finite element, boundary element), as it produces a smaller linear system whose solution requires a fraction of the computational resources; it is easy to implement, robust and stable and is devoid of singularities. The accuracy of the solution depends, however, on various factors: 1) the distribution and number of collocation points and equivalent sources on their respective surfaces, 2) the relative size of the source surface, and 3) configuration symmetry.

It is the purpose of this work to provide additional code validation studies and determine the range of code parameters that produce accurate results with minimal computational costs. Systematic noise prediction studies are presented in which monopole generated incident sound is scattered by simple geometric shapes – spheres (acoustically hard and soft surfaces), oblate spheroids, flat disk, and flat plates with various edge topologies. Comparisons between FSC simulations and analytical results and experimental data are presented.

2. BACKGROUND

2.1. The Fast Scattering Code (FSC)

The FSC has been designed as an aeroacoustic analysis tool for assessing global effects on noise radiation and scattering caused by changes in configuration (geometry, component placement) and operating conditions (background flow, excitation frequency). It can be used as a component of an aircraft system noise prediction package, such as ANOPP II, or as standalone software. Inputs to the code are the scattering surfaces and their impedance, excitation frequency, local density, speed of sound and Mach number, and an incident sound field (generated by the code or provided by the user). The total acoustic field (incident plus scattered) is calculated at a user-specified collection of observers (see Figure 1). Details on the solution methodology and program usage are found in references 1 and 2.

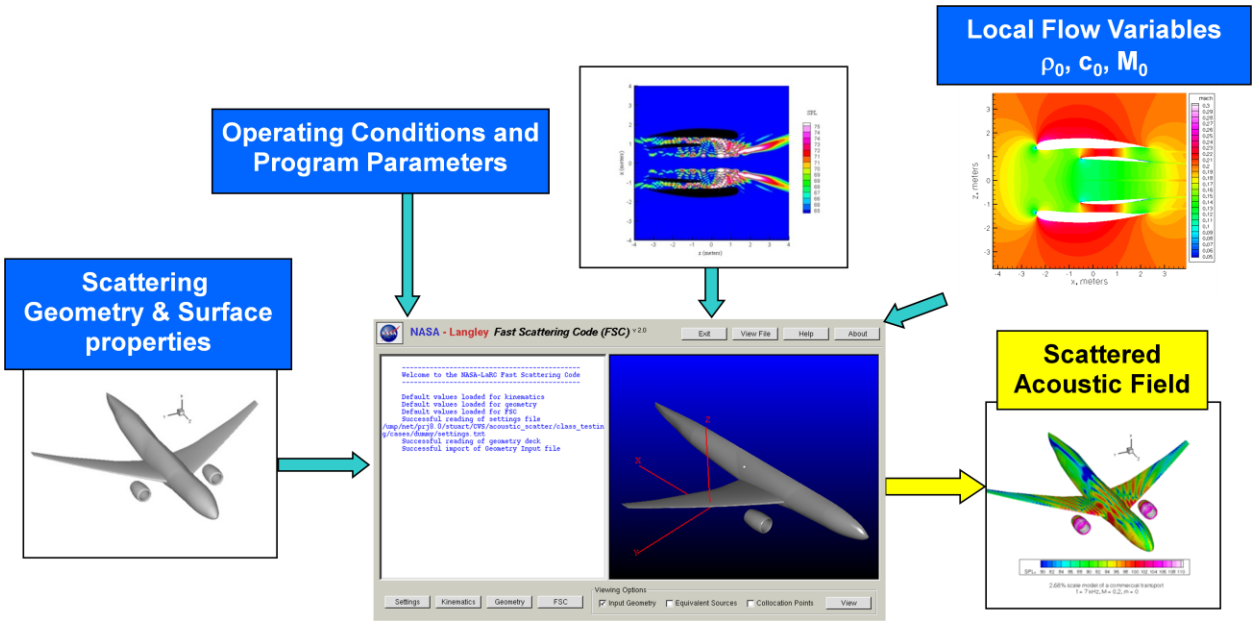

Figure 1.- FSC input/output.

Discretization of the scattering surfaces produces a rectangular system of linear equations of size N_c x N_s (FSC matrix); the procedure, which follows Nyquist frequency limitations, assumes that N_c is proportional to Sk^2 (where S is the surface area of the scatterer, and k the excitation wave number of the incident sound), thus ensuring that the mesh spacing is small enough to capture the incident pressure fluctuations. The proportionality constant depends on a user-selected number of points per wavelength (N_w) and on flow speed. Through numerical experimentation, it has been determined that 1) N_c and N_s should be uniformly distributed on their respective surfaces, and 2) $N_s \sim 1/3\ N_c$ is adequate for the majority of applications. Computer memory consumption for large-scale commercial transports limits the original version of the FSC (v2.0) to problems with moderate excitation frequencies. Simulations for high frequency/large scattering surface area combinations yield immense linear systems that can only be solved with supercomputers and the development of numerical algorithms that drastically reduce computational resource utilization.

In FSC v3.0 the dense, linear least squares solution approach of v2.0 was replaced with an iterative conjugate gradient method (CGM) featuring fast multipole methods (FMM) and fast matrix-vector multiplication algorithms to accelerate matrix solution and field calculations. Benchmarking against results obtained previously with FSC v2.0 indicated that a 95% reduction in computer memory was attained[10], effectively increasing the maximum frequency range achievable for a given configuration using a single processor by a factor of 3. In addition, up to a four-fold reduction in computer time was demonstrated.

Even with the substantial improvements in computer resource utilization achieved with FSC v3.0, simulations of the acoustic field generated by the interaction of very high frequency noise sources and large-scale configurations would require prohibitive amounts of computer memory and time. To obtain solutions within the limits of available computer resources, multi-processor (MP) versions of the FSC have been developed. Both versions feature the use of a CGM iterative

linear algebra solver with direct matrix-vector multiplication; v3.1 uses OpenMP constructs for use in shared memory platforms, and v3.2 includes MPI function calls for use in distributed memory platforms. Every element of the FSC matrix is calculated as needed during each iteration; thus, computer memory requirements are minimal at the expense of longer execution times. Because matrix ill-conditioning may occur during solution of highly symmetrical configurations (see next section), a new option that takes advantage of double symmetry in exterior BVPs has been added to versions 3.1/3.2 (*isym* = 2). The simulations presented in this report made use of this option.

2.1.1. Numerical Instabilities – Symmetry

When applying the ESM to highly symmetrical configurations, advantage should be taken of all possible levels of symmetry to 1) reduce potential problems associated with matrix ill-conditioning caused by the presence of multiple identical elements in the matrix[11], and 2) to make the solution process more efficient. For the purposes of this discussion, a configuration or system consists of all the scattering surfaces of interest plus the source of incident sound.

Consider the sphere/monopole system depicted in Figure 2a – the sphere, of radius a equal to 5.0 meters and centered at the origin, has been discretized such that one hemisphere is the mirror image of the other, with respect to both the x-z and y-z planes: the top half is identical to the bottom half (symmetry about x = 0), and the right half is identical to the left half (symmetry about y = 0). If the acoustic source is placed either on the x or z axis, then the sphere/source system is symmetric (case 1); if the source is moved to any other location, the system is no longer symmetric (case 2). The total (incident plus scattered) acoustic field resulting from the solution of a system consisting of the entire sphere and a source with f = 1000 Hz located 1.0a away from the surface, is depicted in Figure 2b on a 7.5 m radius ring of observers surrounding the sphere: the field is given by the black line for case 1 (source 1 located on the z-axis, as shown in Fig. 2a), and by the red line for case 2 (source 2 located at a point 45^o from the axes in the all-positive octant). Note from the figure that, as expected, the field for case 1 is symmetric with a well-defined shadow zone behind the sphere; for case 2, the acoustic field displays marked asymmetries and incorrect minimum/maximum levels. Most likely, different solutions would be obtained for varying source placements.

For higher source excitation frequencies, at least one level of symmetry must be included in the discretization of the surface if a proper convergence behavior is to be established during solution of highly symmetric systems. This is necessary because the magnitude of the boundary error increases with the number of equivalent sources being used[11]. For case 1 with a hard-wall sphere surface, only one level of symmetry (about y = 0) was sufficient; employing an additional level of symmetry (about x = 0) did not accelerate convergence, but it substantially reduced computer resource utilization by requiring discretization of only one quarter of the sphere. Two levels of symmetry were required for a proper solution of case 1 with an acoustically soft sphere surface – it is surmised that the ill-conditioning of the problem increases with the increased complexity of the surface boundary condition when non-zero admittances are used.

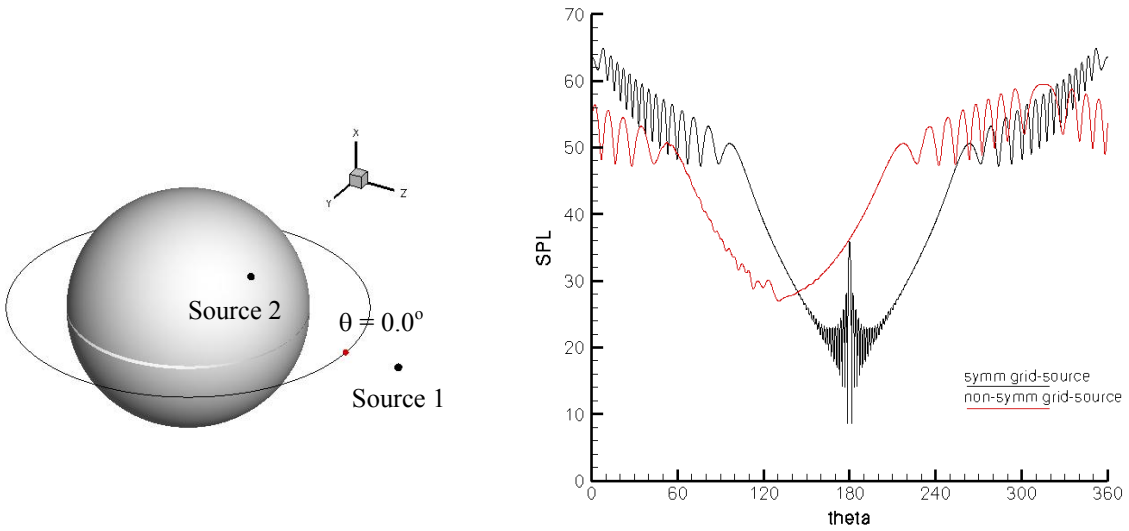

(a) Sphere-source system

(b) Total acoustic field at observer ring

Figure 2. Effects of a non-symmetric grid/source system, f = 1000 Hz, M_∞ = 0.0. Observer field is a 7.5 m radius ring around the sphere.

2.2. Analytical Solution for the Scattering of Sound by a Sphere

The scattering of incident, time harmonic ($e^{+i\omega t}$ time dependence), monopole generated sound by a sound absorbing sphere of constant admittance, A, is governed by the following boundary value problem (BVP):

$$\nabla^2 p' + k^2 p' = \delta(\vec{x} - \vec{x}_0) \quad \vec{x} \in S^+ \tag{1}$$

$$B[p'] \equiv \frac{i}{k\rho_0 c_0}\frac{\partial p'}{\partial n} + Ap' = 0 \quad \vec{x} \in S \tag{2}$$

In (1-2), $k = \omega/c$, $\vec{x}_0$ is the spatial location of the incident monopole ($|\vec{x}_0| > a$), S denotes the sphere surface and S^+ denotes the sphere exterior. It is assumed that the sphere is centered at the origin of the coordinate system and has radius a.

To solve (1-2), the acoustic pressure is split into known incident and unknown scattered parts:

$$p' = p'_{inc} + p'_{scat} \tag{3}$$

The incident pressure is the solution of the Helmholtz equation in unbounded space

$$\nabla^2 p'_{inc} + k^2 p'_{inc} = \delta(\vec{x} - \vec{x}_0) \tag{4}$$

and is given by

$$p'_{inc}(\vec{x}) = \frac{1}{4\pi}\frac{e^{-ikR_0}}{R_0} \qquad R_0 = |\vec{x} - \vec{x}_0|. \tag{5}$$

Combining (1-5), the scattered pressure is the solution of the BVP

$$\nabla^2 p'_{scat} + k^2 p'_{scat} = 0 \quad \vec{x} \in S^+ \tag{6}$$

$$B[p'_{scat}] = -B[p'_{inc}] \quad \vec{x} \in S\,. \tag{7}$$

The spherical geometry of the BVP suggests an expansion of the solution as a series of spherical harmonics. Following the analysis of reference 12 (Section 4.2), the incident pressure is written

$$p'_{inc}(\vec{x}) = \sum_{\nu=0}^{\infty} \sum_{\mu=-\nu}^{\nu} E_\nu^\mu R_\nu^\mu(\vec{x}) \tag{8}$$

where

$$E_\nu^\mu = -ikS_\nu^{-\mu}(\vec{x}_0)\,. \tag{9}$$

$$R_\nu^\mu(\vec{x}) = j_\nu(kr) Y_\nu^\mu(\theta,\varphi) \tag{10}$$

$$S_\nu^\mu(\vec{x}) = h_\nu^{(2)}(kr) Y_\nu^\mu(\theta,\varphi)\,. \tag{11}$$

In (9-10), (r,θ,φ) are spherical coordinates associated with the Cartesian point $\vec{x}$, j_ν are spherical Bessel functions of the first kind, $h_\nu^{(2)}$ are spherical Hankel functions of the second kind, and Y_ν^μ are spherical harmonics given by the formula

$$Y_\nu^\mu(\theta,\varphi) = (-1)^\mu \sqrt{\frac{(2\nu+1)(\nu-|\mu|)!}{4\pi(\nu+|\mu|)!}} P_\nu^{|\mu|}(\cos\varphi) e^{i\mu\theta} \tag{12}$$

where $P_\nu^{|\mu|}$ are Legendre functions of degree ν and order $|\mu|$.

The scattered pressure is written as a superposition of singular harmonics

$$p'_{scat}(\vec{x}) = \sum_{\nu=0}^{\infty} \sum_{\mu=-\nu}^{\nu} C_\nu^\mu S_\nu^\mu(\vec{x}) \tag{13}$$

where the unknown coefficients C_ν^μ are determined from the boundary condition (7) and the incident sound expansion (8). Let

$$\sigma = -ik\rho_0 c_0 A\,, \tag{14}$$

then

$$C_\nu^\mu = -\frac{j'_\nu(ka) + \sigma k^{-1} j_\nu(ka)}{h_\nu^{(2)\prime}(ka) + \sigma k^{-1} h_\nu^{(2)}(ka)} E_\nu^\mu \tag{15}$$

Special function routines for calculating the formulas in (1-15) were taken from user supplied software of reference 13.

2.3. Configuration Description

2.3.1 Spheroids

An important goal of the study was to assess the effects of excitation frequency and surface shape on shadow zone characteristics for similar geometries. To this end a sphere, two oblate spheroids of decreasing thickness, and a thin flat disk with a rounded edge, were placed with respect to the acoustic source so as to project the same geometric zone of silence. The configurations are depicted in Figure 3. The sound generator was a stationary monopole of unit strength located at (0, 0, 10) meters. The sphere was centered at the origin, and had a radius r equal to 5.0 meters. The oblate spheroids (OS1 and OS2), also centered at the origin, were generated by adjusting the length of the semi-major (a) and semi-minor (b) axes of the sphere. Geometric characteristics for the scattering bodies are given in Table 1.

Table 1. – Geometric data for oblate spheroids.

Configuration	Geometrical Parameters, m	Source Surface Size
Sphere	$r = a = 5.0$	$0.9r$
Oblate Spheroid 1 (OS1)	$a = 5.77$, $b = 1.147$	$0.80b$
Oblate Spheroid 2 (OS2)	$a = 5.77$, $b = 0.38$	$0.40b$
Flat Disk (rounded edge)	$r = 4.33$, $t/D = 0.035$	$0.033t$

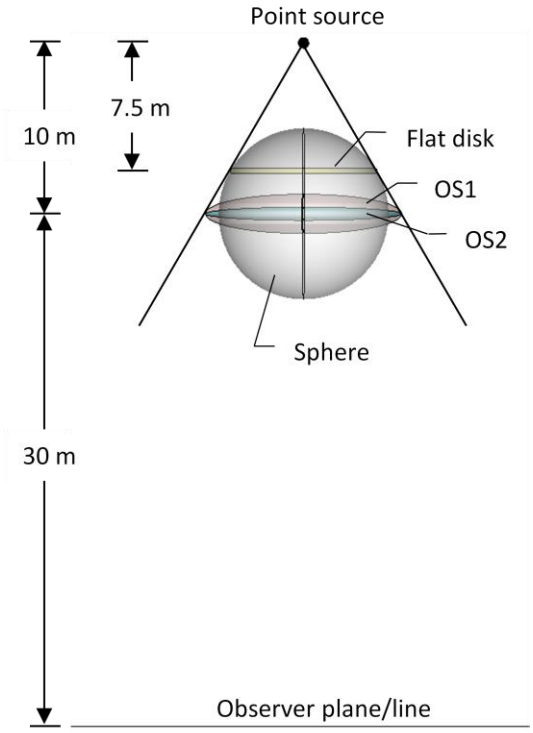

Figure 3.- Oblate spheroid geometries and their relative placement.

2.3.1.1 Source Surface Construction

The geometry module of the FSC is used to 1) discretize the scattering surfaces into N_c collocation points, and 2) generate/discretize the source surfaces into N_s equivalent sources. For simplicity, the module generates source surfaces by creating smaller versions of the scatterers utilizing a single user-supplied scaling parameter, *srcalpha*. The main disadvantages of using only one scaling parameter are that 1) portions of the source surface may not be interior to the scattering body, thus violating a requirement of the ESM for exterior BVPs; and 2) large localized differences in source surface size, relative to the scattering body, arise for elongated geometries. To alleviate these effects, the source surface is anchored to the scattering body at the leading and trailing edges for wing-like structures consisting of a collection of airfoils (wings, nacelles, pylons, blended wing bodies), and at the nose and tip for structures composed of two – top and bottom – arbitrarily shaped halves (fuselages, spheres, cylinders, etc.). The size and shape of the resulting source surface can substantially affect the quality of a solution.

Source surface size – An adequate source surface size depends on the excitation frequency of the incident sound, and on the shape/surface area of the scatterer. In general, for moderate to high frequencies and relatively large, thick bodies, *srcalpha* ~ 0.9 to 0.95 gives excellent results; the thinner the body and the lower the frequency, the smaller *srcalpha* should be. For example, *srcalpha* ~ 0.75 to 0.8 works well for nacelles at most frequencies of interest; for very thin shapes, *srcalpha* ≤ 0.1. Source surface sizes for the spheroids used in the study are included in Table 1.

Source surface shape – Ideally, a constant separation between source and scattering surfaces should be maintained. This is precluded in the regions where the source surface is anchored to the scattering body. Most geometries of interest are composed of wing-like structures and/or fuselages; for these, the effects of non-constant separation at the edges are small. For canonical shapes like spheres, spheroids, cylinders, and cubes, the effect is more pronounced. In these cases, the geometry module can still be used advantageously by employing separate, properly constructed scattering and source surfaces as inputs. The procedure is as follows. First, using the scattering surface as input, obtain the collocation points (N_{c1}). Run the module again, using a smaller replica of the scattering surface (scaled so as to meet source surface size requirements) as input, to obtain a second set of collocation points (N_{c2}). Note that by adjusting the number of points per wavelength (N_w) on the second run, $N_{c2} \sim 1/3\ N_{c1}$. Thus, N_{c2} will be used as equivalent sources in a subsequent ESM module run (the two sets of equivalent sources generated by the geometry module are discarded). This approach was followed to discretize the sphere surfaces; for consistency, it was also employed with the oblate spheroids – the geometric definitions of the source surfaces were created by adjusting the scale in every dimension to maintain an approximately constant separation to the parent scattering surface.

To correctly solve exterior BVPs, the ESM requires sufficient space inside the scattering body for the placement of a suitable source surface – a certain minimum thickness for the scatterer is necessary. It was found during the present study that, as expected, it is quite difficult to obtain well behaved solutions for very thin oblate spheroids (maximum thickness ratio $(t/D)_{max} < 0.04$), the reason being extreme thinness toward the edge. This problem was eliminated by considering a constant thickness, flat disk with a rounded edge. The resulting geometry (see Fig. 3 and Table 1) had a smaller $(t/D)_{max}$ than that achievable for oblate spheroids.

Because all the configurations or systems (scatterer plus incident sound generator) considered here are symmetric with respect to both the x-z and y-z planes, only one quarter of each surface was discretized, and two levels of symmetry were used to obtain the scattered acoustic fields.

2.3.2. Flat Plate

The last configuration to be considered in the study was a relatively small flat plate with different edge geometries (square, rounded, sharp). The dimensions of the plate were 0.5 m x 2.0 m. The acoustic source, a stationary monopole of unit strength, was placed 0.25 m from the center of the surface. The plate dimensions, the type, location, and frequencies of the sound generator, as well as the observer field location, were chosen to represent a subset of the configurations tested in reference 14.

2.3.2.1 Source Surface Construction

For a given scatterer, N_c, N_s, and the relative size of the source surface are frequency dependent. In general, the size of the source surface necessary to obtain a good solution decreases with frequency, scattering body thickness, and distance to the acoustic source. Thus, it was decided to select the plate thickness so that a correct solution for the lowest frequency of interest could be obtained, and use the same geometry for the higher frequencies. This resulted in a plate with a thickness of 0.07 m, and a 0.006 m thick source surface. In order to maintain the slope discontinuities at the edges inherent in the geometry, the surfaces were defined as multi-component entities; as was done with the spheroids, each surface (scattering and source) was discretized separately using only one quadrant, and two levels of symmetry were used during execution of the ESM module.

3. RESULTS AND DISCUSSION

All results presented in this report were obtained using two levels of symmetry[*], and stationary monopoles as equivalent sources. The configurations were immersed in a quiescent flow (M_∞ = 0.0). The simulations were conducted in the NAS Columbia super computer using FSC v3.1 for most of the frequency range; because it has better scalability, FSC v3.2 was used for the highest frequency cases. The runs were stopped after reaching either the user supplied tolerances for two of the convergence metrics employed in the code (L2 norms of the solution vector residual and the source strength vector, set to 1.0×10^{-5} and 1.0×10^{-6}, respectively), or enough iterations to properly resolve the shadow zone.

3.1. Sphere

The excitation frequencies, f, considered in the exercise covered the range of Helmholtz number $1 < ka < 500$. These frequencies are listed in Table 2. Also included in the table are grid (matrix) sizes and metrics at each frequency of interest, as well as computer resource utilization statistics. FSC versions 3.1/3.2 have been optimized for high frequency/large scale applications. The use of v3.1 to solve the low frequency scattering problems presented here ($f < 1000$ Hz) was done for consistency only, as the computer resources (processors and time) required to obtain a converged

[*] Superposition of the acoustic fields is assumed when using symmetry. If the acoustic source lies on a symmetry plane, its strength is doubled. Thus, 6 dB per plane of symmetry must be removed from the solution to account for this fact.

solution for such small cases will certainly exceed those of FSC v2.0 – results from a comparison test (not shown) using a matrix of size N_c x N_s ~ 3500 x 1200 indicated that the single-processor v2.0 is approximately 17 times faster than v3.1 with 10 processors. Thus, the execution times presented in Table 2 for the two lowest frequencies should not be used to assess code performance.

The total acoustic field was sampled at 1) a plane bisecting the configuration, 2) a straight line 60 meters long and located at z = -30 m (8*a* away from the source), and 3) a ring placed around the sphere, centered at the origin, with a radius r = 7.5 m (1.5*a*); on this ring, $\theta = 0^o$ corresponds to the point closest to the source (see Fig. 2a). An analytical approximation for the noise scattered by a single sphere with an acoustically hard or soft surface, based on spherical harmonic expansions (see section 2.2), was used to validate the simulations for the straight line and ring observer fields; the number of terms included in the spherical harmonic expansions, *nn*, is also provided in Table 2. Two surface impedance cases have been considered, namely, a hard-wall sphere with admittance $A = 0.0 + 0.0i$ rayl^{-1}, and an acoustically soft sphere with $A = 9.0 \times 10^{-4} + 9.0 \times 10^{-4} i$ rayl^{-1}. The latter admittance is within the range of values used in engine liner design.

Table 2. – Acoustic source excitation frequencies, grid metrics, and execution time statistics for sphere scattering.

Frequency, Hz	***ka***	**Grid size, (N_c x N_s)**	**Points per wavelength, N_w**	**Processors used, N_{proc}**	**Number of iterations, N_{iter}**	**Execution time, t_{exec} hours/job**	**Terms in analytic expression, *nn***
11	1.0	196 x 65	50.00	4	19	9.478×10^{-5}	50
541	50.0	4940 x 1688	5.00	16	114	4.067×10^{-2}	100
1000	92.4	16997 x 5548	5.00	64	354	1.964×10^{-1}	100
1623	150.0	33346 x 9858	4.32	64	305	8.470×10^{-1}	175
2164	200.0	67906 x 22150	4.62	64	1800	2.035×10^{1}	250
3247	300.0	180192 x 58570	5.00	64	1500	1.343×10^{2}	325
4329	400.0	500669 x 162850	6.00	64	1113	7.011×10^{2}	N/A
5411	500.0	720890 x 162224	6.00	128	680	3.355×10^{2}	N/A

3.1.1 Acoustically Hard Surface

In general, surface discretization using $5 < N_w < 12$ is sufficient to properly capture the physics in the vast majority of scattering problems. However, this rationale does not apply to very low frequencies, where the wavelength of the sound is larger than the dimensions of the body. In such cases, a minimum of a few hundred points is necessary for an adequate definition of the scattering surface of interest. For the lowest excitation frequency considered in the study, 11 Hz (*ka* = 1), surface discretization was performed using N_w = 50, resulting in N_c ~ 200. The total (incident plus scattered) acoustic field at this frequency, sampled at the three observer groups described previously, is presented in Figure 4. Sound pressure level (SPL) contours for a plane bisecting the configuration are presented in Fig. 4a – note that, as expected, the omni-directional incident sound field is only minimally disturbed by the presence of the sphere. On a ring surrounding the body (Fig. 4c), the spherically radiating nature of the acoustic field is apparent, with minor differences between incident and total components. Plane wave propagation is almost fully established by the time the sound reaches a line 40 meters away from the source (Fig. 4d); at this distance, the differences between incident and total acoustic fields are very small,

indicating negligible scattering by the sphere. Note from the latter two figures that agreement between FSC and analytic results is excellent. Also included as Figure 4b are iteration history plots for the convergence metrics – observe that the solution reached user specified tolerances very rapidly.

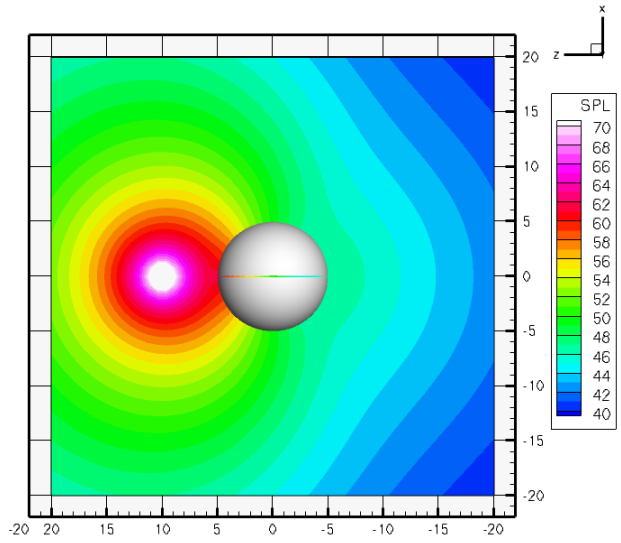

(a) Plane bisecting the configuration

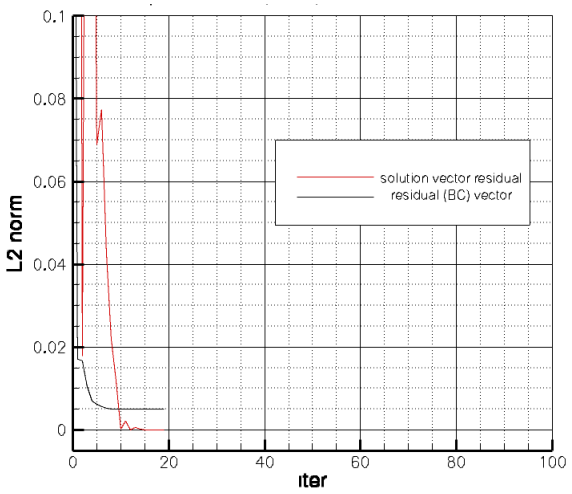

(b) Convergence history

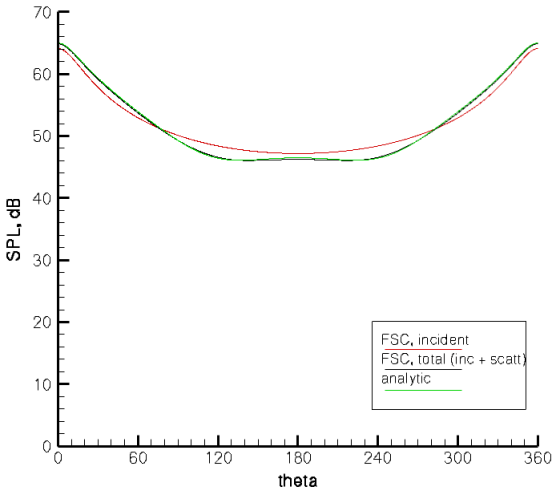

(c) Ring surrounding sphere

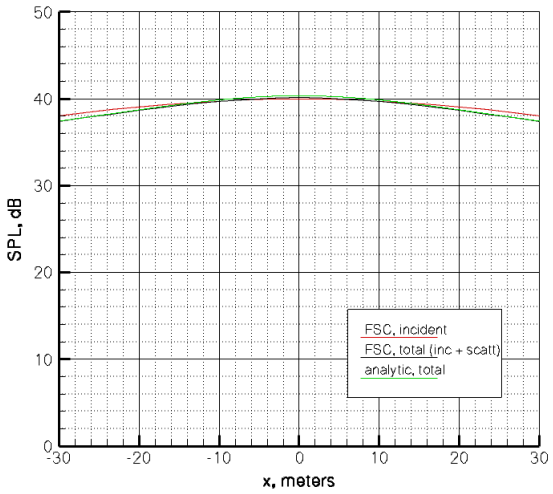

(d) Observer line at z = -30 m

Figure 4. Total acoustic field for sphere/point source system, f = 11 Hz (ka = 1), M_∞ = 0.0.

Observer field results for f = 541 Hz are presented in Figure 5. Note from Fig. 5b that the FSC solution reached steady levels very quickly, converging to specified tolerances after about 100 iterations. SPL contours on a plane bisecting the system (Fig. 5a) indicate that there is substantial scattering of sound by the sphere, giving rise to a well defined shadow zone behind the body. The symmetric and highly oscillatory nature of the total acoustic field is clearly observed in Figures 5c and 5d, where the incident field (in the absence of scattering surfaces) is provided for reference purposes. On a ring surrounding the sphere (Fig. 5c), shielding effects are obvious for

$90^o < \theta < 270^o$, indicating the boundaries of the shadow zone. Within this region, the total sound decreases and then increases as it reaches the point on the ring farthest from the source (θ = 180^o), where its amplitude is still several dB lower than that of the incident field. On a line 40 m away from the source (Fig. 5d), shielding causes the total noise to decrease and then increase as the observer moves toward the sphere, peaking at the point closest to the body. At this point, the total noise level is slightly higher than that of the incident field. Note from the line plots that agreement between FSC and analytic results is excellent. It is not known at present if the "singularity" at points in the shadow zone directly opposite the source has a physical meaning.

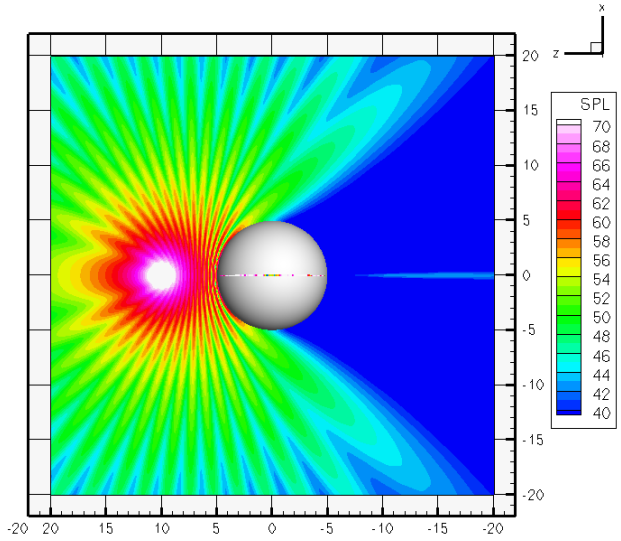

(a) Plane bisecting the configuration

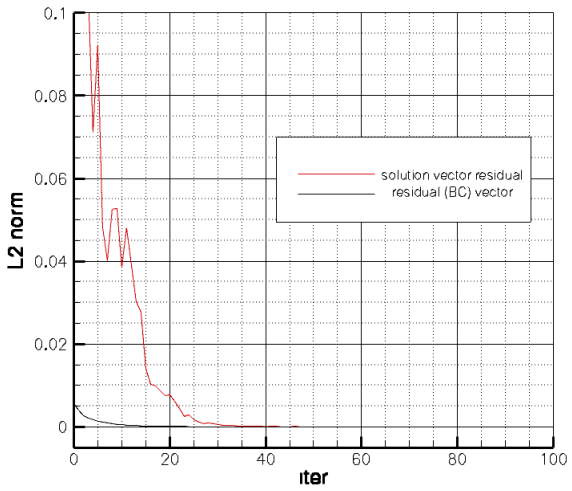

(b) Convergence history

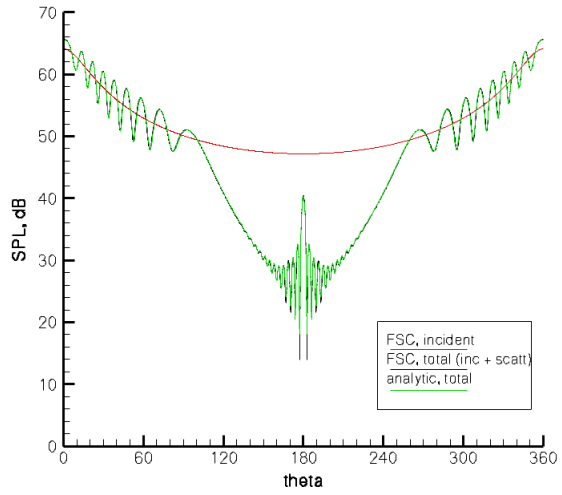

(c) Ring surrounding sphere

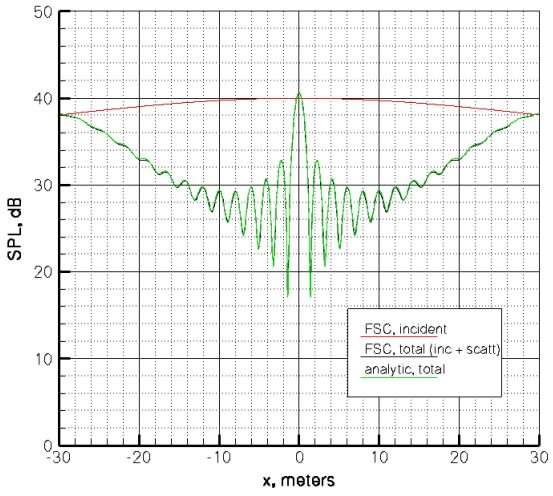

(d) Observer line at z = -30 m

Figure 5. Total acoustic field for sphere/point source system, f = 541 Hz (ka = 50), M_∞ = 0.0.

Observer field results for f = 1000 Hz (ka = 92.4) are presented in Figure 6. Note from Figure 6b that the FSC solution is well converged after a few hundred iterations. SPL contours on a plane bisecting the configuration are given in Fig. 6a; note that a clearly defined shadow zone behind

the sphere is present. Comparisons between FSC results and those obtained from the analytical solution are given in Figures 6c and 6d for the ring and straight line observer fields, respectively. Note from the figures that the solutions are symmetric and highly oscillatory, as expected, and practically identical – the SPL values at the ring of observers (Fig. 6c) clearly indicate that the shielding effect is substantial, manifested by a 52 dB drop in noise between highest and lowest levels. The line of observers (Fig. 6d) indicates that, at 40 meters away from the source, the total noise is highest at the points most distant from the sphere, decreases as shielding by the sphere increases, and peaks again at the point closest to the sphere, where the level is comparable to that at both ends of the line.

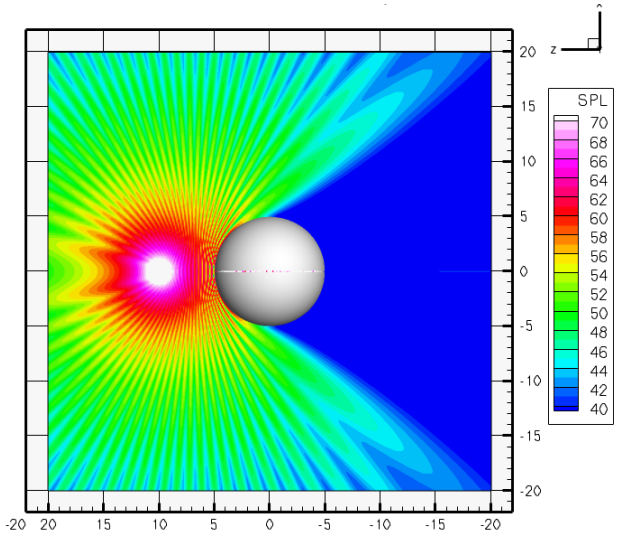

(a) Plane bisecting the configuration

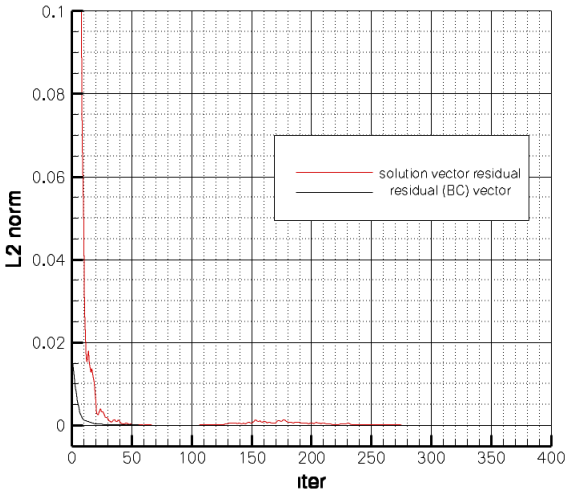

(b) Convergence history

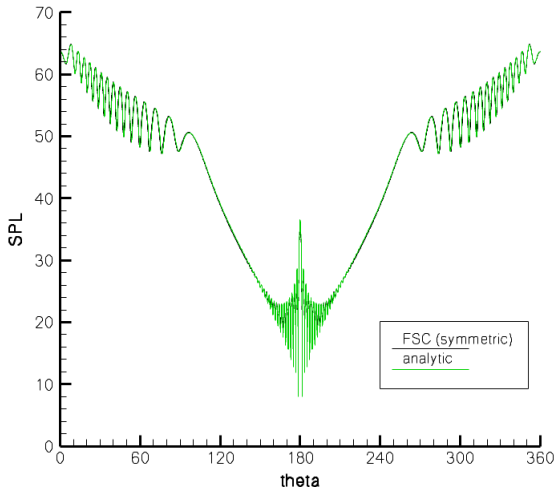

(c) Ring surrounding sphere

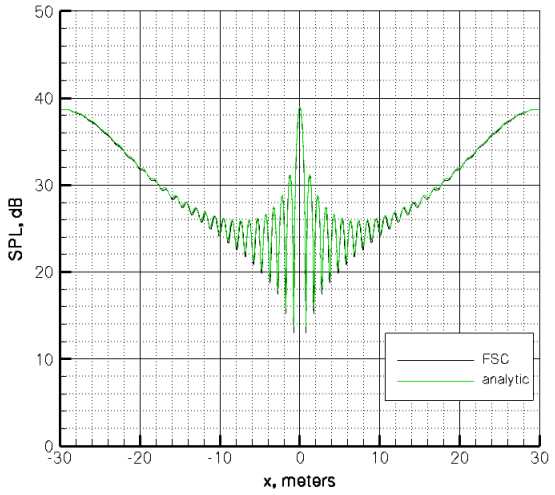

(d) Observer line at z = -30 m

Figure 6. Total acoustic field for sphere/point source system, f = 1000 Hz (ka = 92.4), M_∞ = 0.0.

Solution convergence histories and observer field comparisons for an excitation frequency of 1623 Hz are depicted in Figure 7. As before, excellent FSC convergence is achieved within a few hundred iterations (Fig. 7b). The trends are very similar to those observed at the lower

frequencies (once scattering becomes evident) – the oscillatory nature of the total field is apparent, with the added effect of improved shielding as a result of shorter wavelengths (Figs. 7c and 7d). The latter is manifested as a larger noise differential within the shadow zone. Also note that, as before, agreement between FSC and analytical results is remarkable.

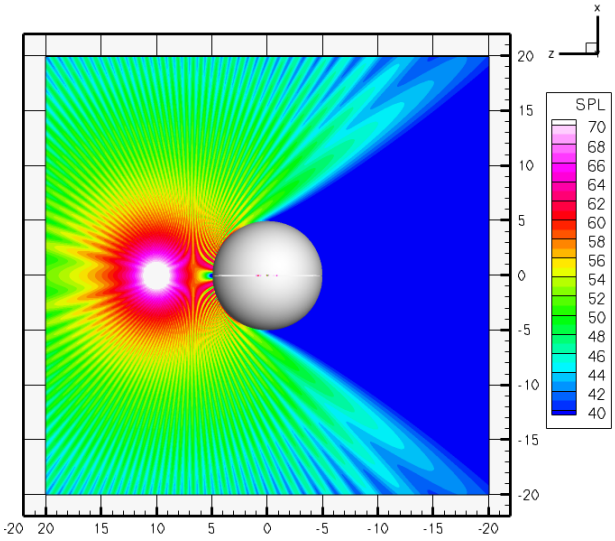

(a) Plane bisecting the configuration

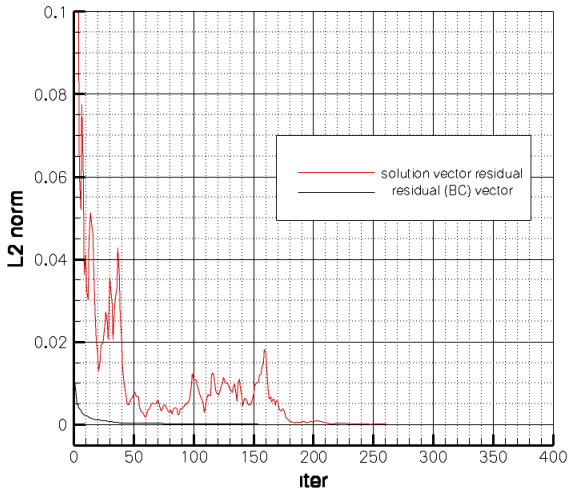

(b) Convergence history

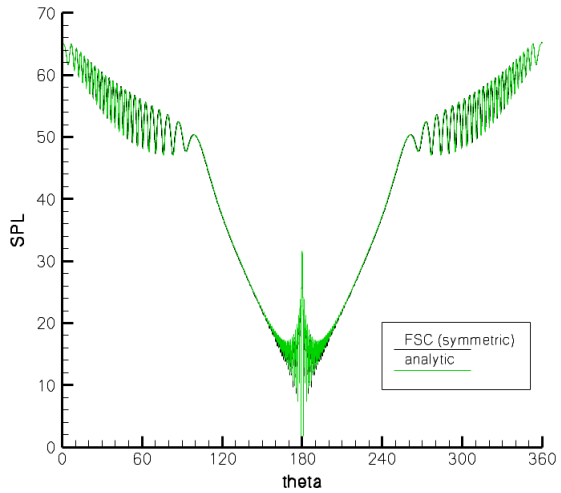

(c) Ring surrounding sphere

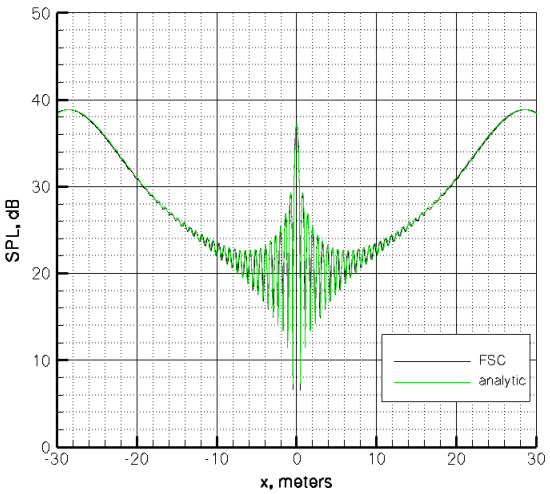

(d) Observer line at z = -30 m

Figure 7. Total acoustic field for sphere/point source system, f = 1623 Hz (ka = 150), M_∞ = 0.0.

The amount of noise shielding by the sphere increases with frequency, as can be observed in Figures 8 and 9, which present the acoustic fields for f = 2164 Hz (ka = 200) and f = 3247 Hz (ka = 300), respectively. It was also noted during this exercise that the portion of the total acoustic field where noise amplification occurs due to reflections from the sphere surface converges very rapidly, independent of frequency; however, as the frequency increases, substantially more iterations and/or denser grids (increased N_w during surface discretization) may be necessary to fully converge the portion of the field in the shadow zone. Observe from Table 2 that, in general,

$N_w \sim 5$ sufficed to obtain very good agreement between FSC and analytical results, but noticeably more iterations were required for the higher frequencies, as seen in Figures 8b and 9b.

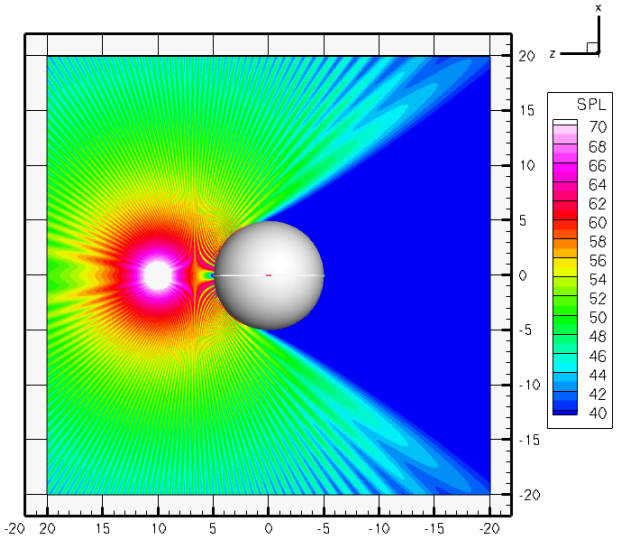

(a) Plane bisecting the configuration

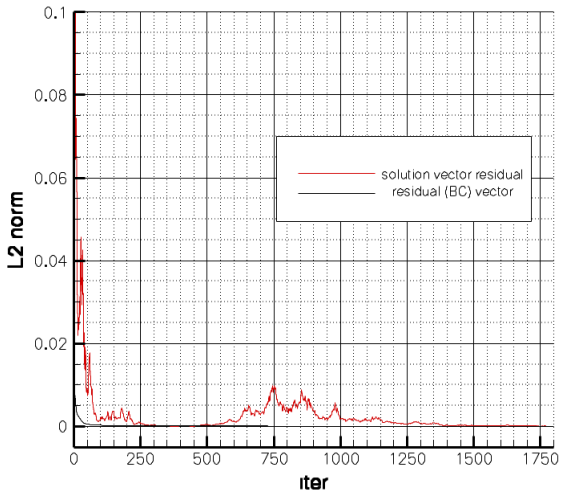

(b) Convergence history

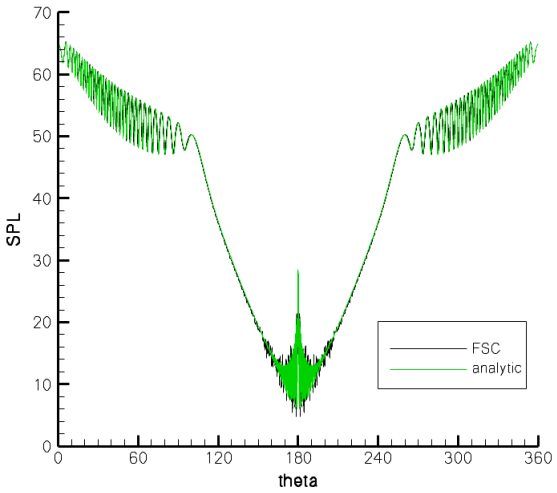

(c) Ring surrounding sphere

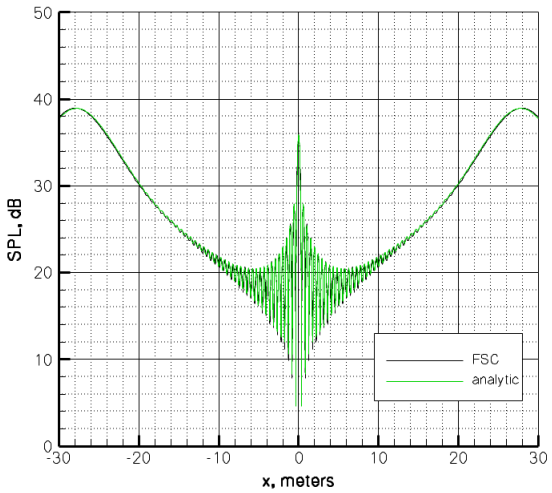

(d) Observer line at z = -30 m

Figure 8. Total acoustic field for sphere/point source system, $f = 2164$ Hz ($ka = 200$), $M_\infty = 0.0$.

FSC interim solution convergence histories and observer field plots for $f = 4329$ Hz ($ka = 400$) are presented in Figure 10; no analytical solution could be obtained at this frequency because of convergence problems[†]. Although the trends observed previously are already well established, it is apparent that more iterations are necessary if a better resolution of the acoustic behavior in the shadow zone is desired. The line fields are expected eventually to collapse to patterns similar to those obtained for the lower frequencies; however, because of the large size of the problem and

[†] Convergence problems with the analytical expression derived in section 2.2 were encountered for the higher frequency cases $ka = 400$ and 500. The problems were traced to the Legendre function calculations in the reference 2 software. Alternate Legendre function software was not considered for this exercise.

the fact that a considerable noise differential already exists in the shadow zone, the use of additional computer resources for this simulation cannot be justified. A solution using $N_w = 5$ was also obtained for this frequency; those field results (not shown) indicated that the shadow zone was slightly less resolved at the same stage in the solution process. In hindsight, it may have been more efficient to continue that solution than to start a new one on a denser ($N_w = 6$) grid. Similar observations apply to the field plots for $f = 5411$ Hz ($ka = 500$), depicted in Figure 11.

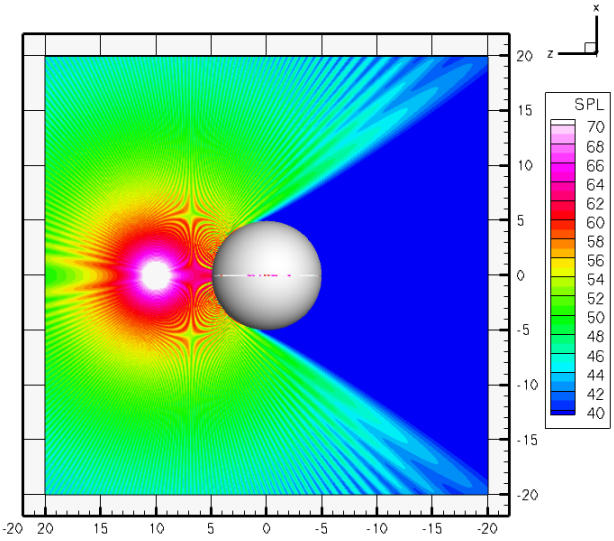

(a) Plane bisecting the configuration

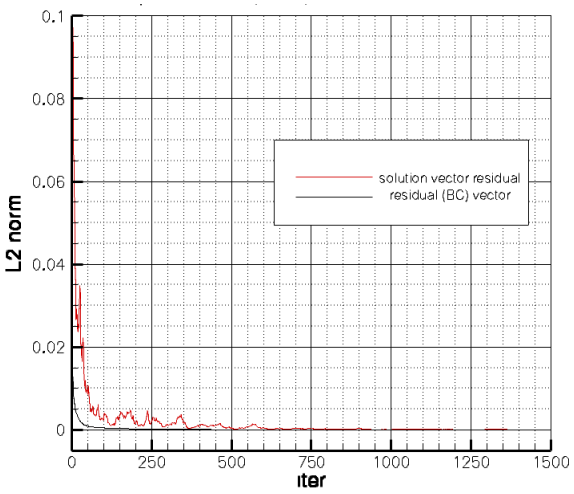

(b) Convergence history

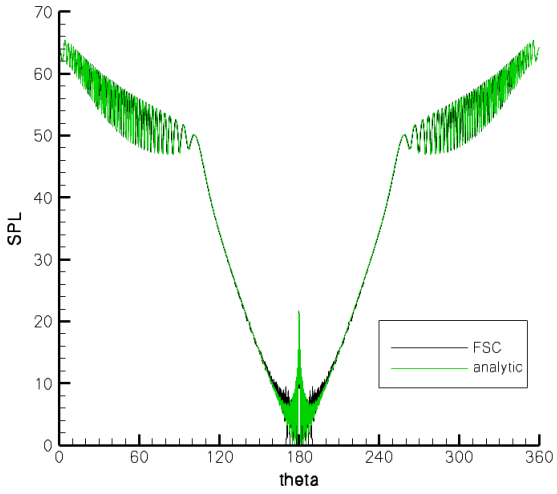

(c) Ring surrounding sphere

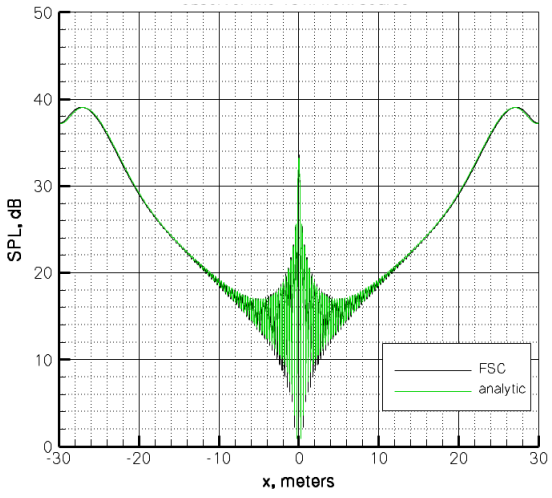

(d) Observer line at z = -30 m

Figure 9. Total acoustic field for sphere/point source system, $f = 3247$ Hz ($ka = 300$), $M_\infty = 0.0$.

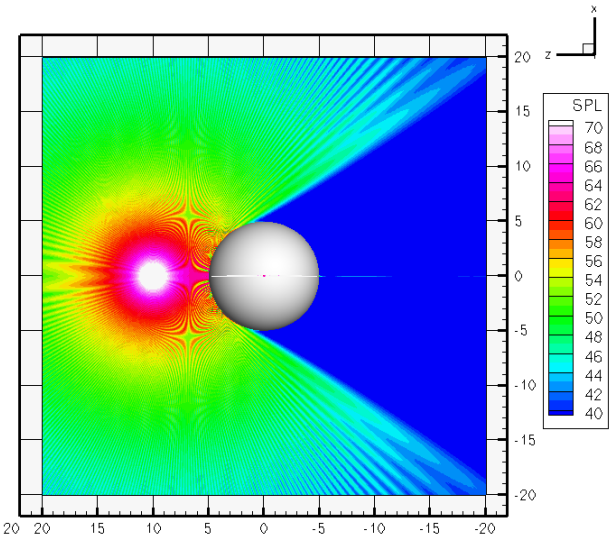

(a) Plane bisecting the configuration

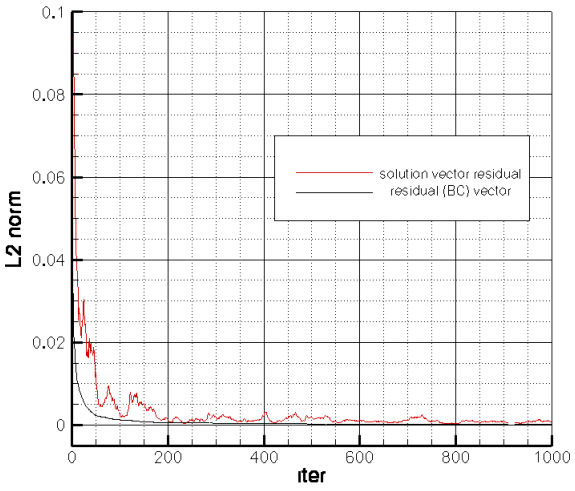

(b) Convergence history

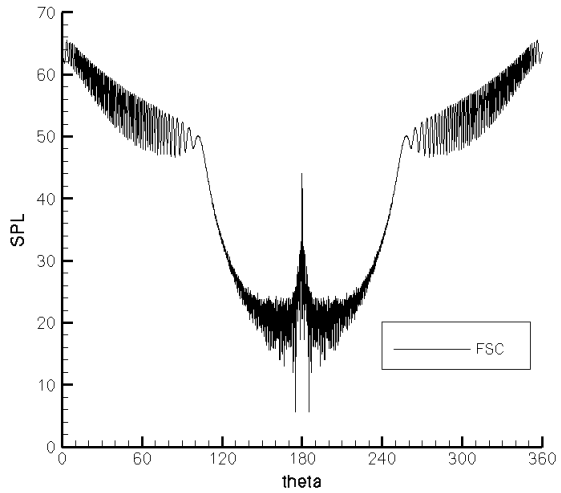

(c) Ring surrounding sphere

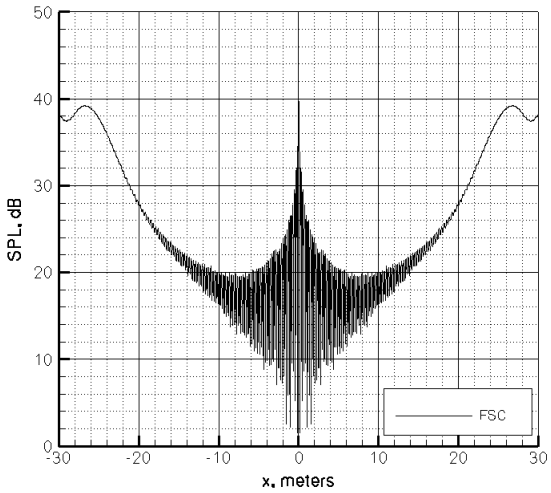

(d) Observer line at z = -30 m

Figure 10. Total acoustic field for sphere/point source system, f = 4329 Hz (ka = 400), M_∞ = 0.0.

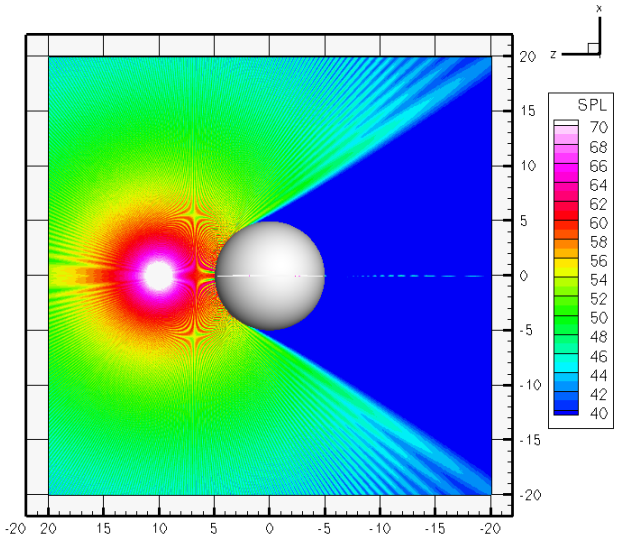

(a) Plane bisecting the configuration

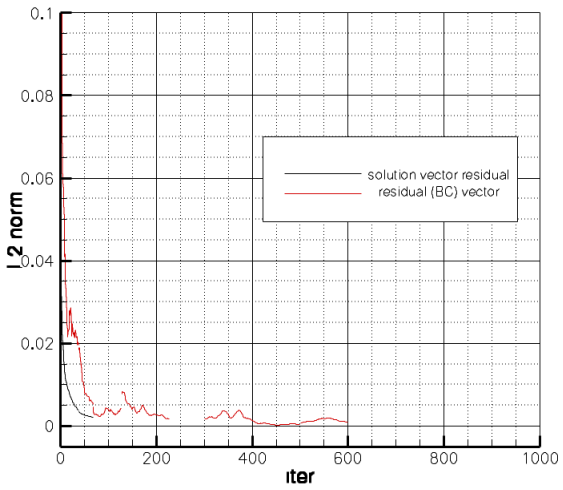

(b) Convergence history

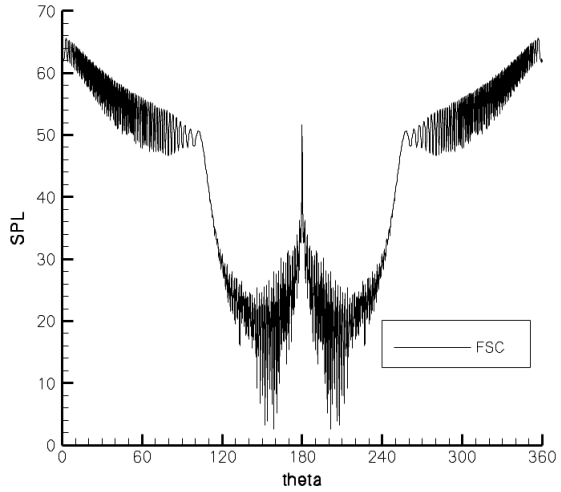

(c) Ring surrounding sphere

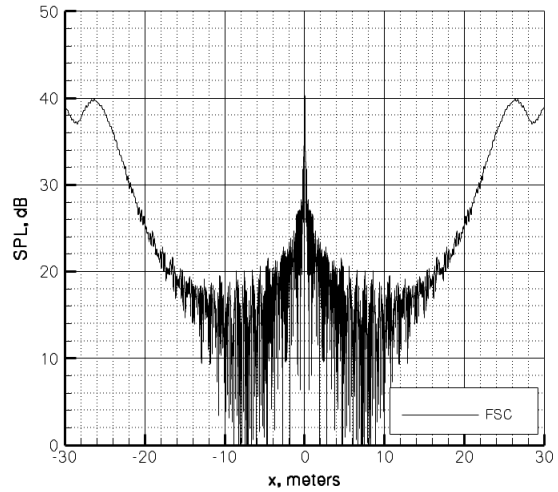

(d) Observer line at z = -30 m

Figure 11. Total acoustic field for sphere/point source system, f = 5411 Hz (ka = 500), M_∞ = 0.0.

3.1.2. Acoustically Soft Surface

The total acoustic field on a ring (r = 7.5 m) placed symmetrically around a lined sphere is provided in Figures 12 and 13 for f = 1000 Hz and f = 1623 Hz, respectively. The entire surface of the body has been acoustically treated (**A** = 9.0e-04 + 9.0e-04i rayl^{-1}). Note from Figs. 12a and 13a that the treated surface substantially absorbs the noise radiated by the source, as manifested by an enhanced noise differential in the shadow zone[‡]. As observed previously for the hard-wall case, the "depth" of the shadow zone increases with frequency. A comparison between FSC and analytic results for f = 1000 Hz is presented in Fig. 12b. Note that the agreement between the two

[‡] Although negative SPL values do not have practical significance, they represent acoustic pressures below the reference value, 2.0 x 10^{-5} Pa.

solutions is excellent, with only minor differences in the "zone of silence" below the threshold of human hearing. A converged analytic solution for f = 1623 Hz could not be obtained.

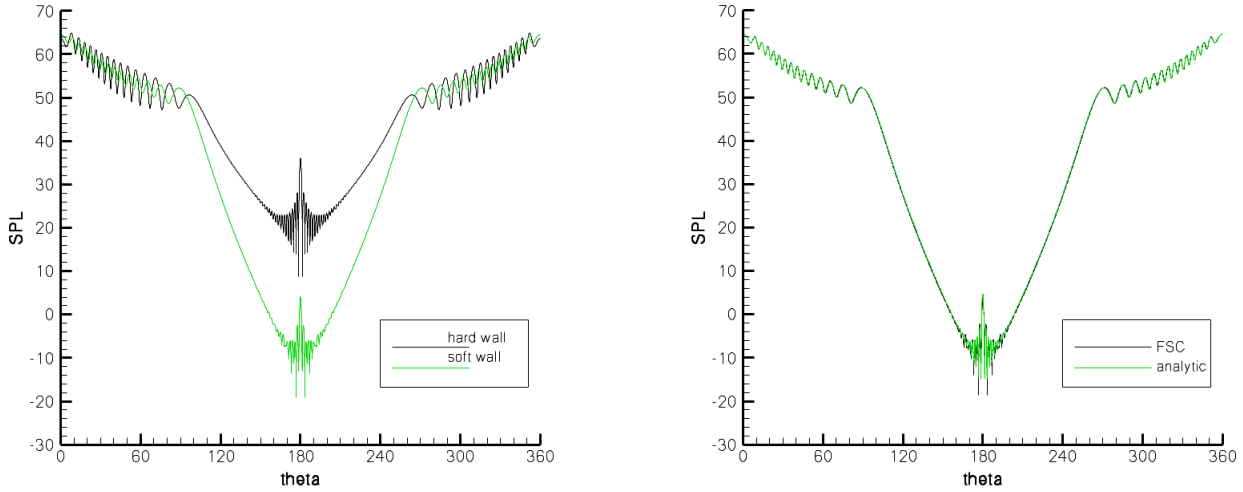

(a) Liner effects (b) Comparison with analytic results

Figure 12. Total acoustic field on a 7.5 m radius ring surrounding a lined sphere; f = 1000 Hz, M_∞ = 0.0, A = 9e-04 +9e-04i.

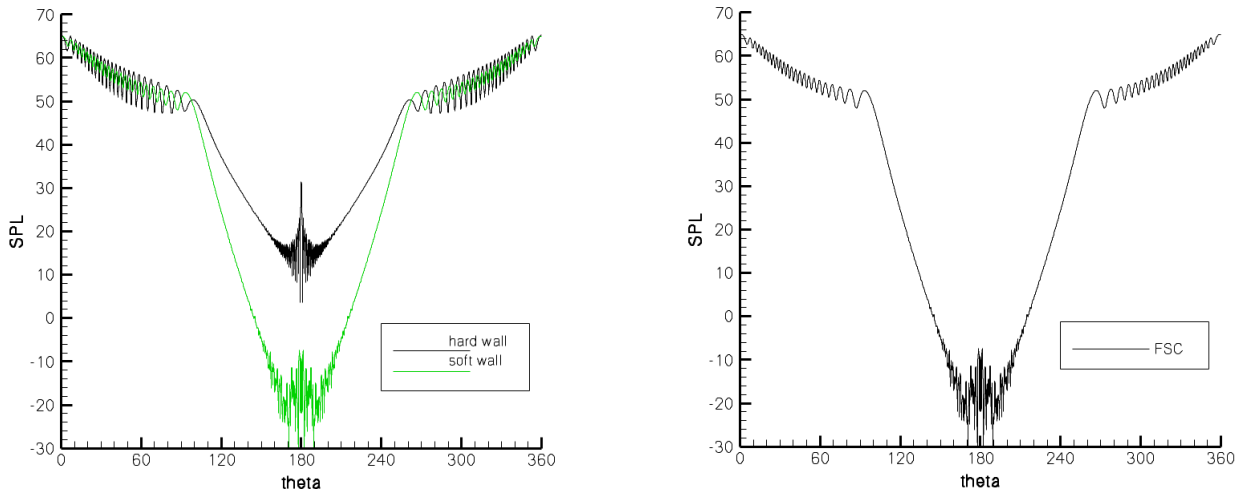

(a) Liner effects (b) Comparison with analytic results

Figure 13. Total acoustic field on a 7.5 m radius ring surrounding a lined sphere; f = 1623 Hz, M_∞ = 0.0, A = 9.0 x 10^{-4} + 9.0 x $10^{-4}i$ rayl^{-1}.

3.2 Oblate Spheroids

The source excitation frequencies considered for the spheroids and flat disk were similar to those used for the sphere cases; these frequencies, along with other grid metrics, are given in Table 3. Execution time statistics are provided in Table 4; the observations made for the sphere cases with regard to low frequency resource allocation (see section 3.1) apply to the oblate spheroids as well. The total acoustic field was sampled at 1) a 60 m x 60 m plane bisecting the configuration,

2) a 60 m x 60 m plane located at z = -30 m, 3) a line formed by the intersection of the two planes, and 4) a ring placed around the configurations, centered at the origin, with a radius r = 7.5 m; on this ring, $\theta = 0^o$ corresponds to the point closest to the source. Only acoustically hard surfaces were considered.

Table 3. – Acoustic source excitation frequencies and grid metrics for oblate spheroids.

Frequency, Hz	*ka*	OS1		OS2		Flat Disk	
		Grid size, (N_c x N_s)	N_w	Grid size (N_c x N_s)	N_w	Grid size (N_c x N_s)	N_w
11	1.0	174 x 56	55.00	161 x 52	55.00	156 x 52	70.00
541	50.0	3322 x 1173	5.00	3360 x 1089	5.00	1954 x 620	5.00
1000	92.4	12443 x 4042	5.00	11580 x 3860	5.00	6718 x 2104	5.00
1623	150.0	32870 x 10655	5.00	30504 x 9838	5.00	17710 x 5789	5.00
2164	200.0	58364 x 19527	5.00	54315 x 18068	5.00	31430 x 10480	5.00
3247	300.0	131344 x 42504	5.00	122100 x 39234	5.00	70882 x 23156	5.00
4329	400.0	233914 x 78212	5.00	217364 x 72195	5.00	126160 x 42372	5.00

Table 4. – Execution time statistics for oblate spheroids.

Frequency, Hz	*ka*	OS1			OS2			Flat Disk		
		N_{proc}	N_{iter}	t_{exec}, hours/job	N_{proc}	N_{iter}	t_{exec}, hours/job	N_{proc}	N_{iter}	t_{exec}, hours/job
11	1.0	32	19	9.828×10^{-5}	16	44	1.575×10^{-4}	16	75	2.415×10^{-4}
541	50.0	32	89	1.310×10^{-2}	16	70	1.103×10^{-2}	16	209	1.521×10^{-2}
1000	92.4	64	626	2.971×10^{-1}	32	166	1.497×10^{-1}	16	278	1.753×10^{-1}
1623	150.0	64	932	2.452	64	508	1.291	32	1000	1.537
2164	200.0	64	1812	1.471×10^{1}	64	1000	6.797	32	1000	4.820
3247	300.0	64	1500	6.272×10^{1}	64	1000	3.831×10^{1}	64	1000	1.206×10^{1}
4329	400.0	128	1000	7.114×10^{1}	128	1000	5.948×10^{1}	128	1000	1.952×10^{-1}

Total acoustic fields at two intersecting planes are presented in Figure 14 for the sphere and OS1, and in Figure 15 for OS2 and the flat disk. The excitation frequency is 1000 Hz. Several general observations can be made regarding the sound scattering characteristics of each configuration. Note from the figures that the oblate spheroids generate larger, stronger shadow zones: they are more effective at shielding monopole noise than the sphere or flat disk. Of the two, OS1 is slightly better. Because of enhanced diffraction as the sound waves encounter the surface, the sphere projects the smallest shadow zone. Also note that the sound in the amplification zone has shorter wavelength for the spheroids and disk than for the sphere; this is most likely caused by enhanced reflection from the flatter surfaces. A region of relatively high sound amplitude can be observed in the shadow zone opposite to the acoustic source. This behavior is intrinsic to the solution of electromagnetic and acoustic radiation scattering by spheres, spheroids and disks.

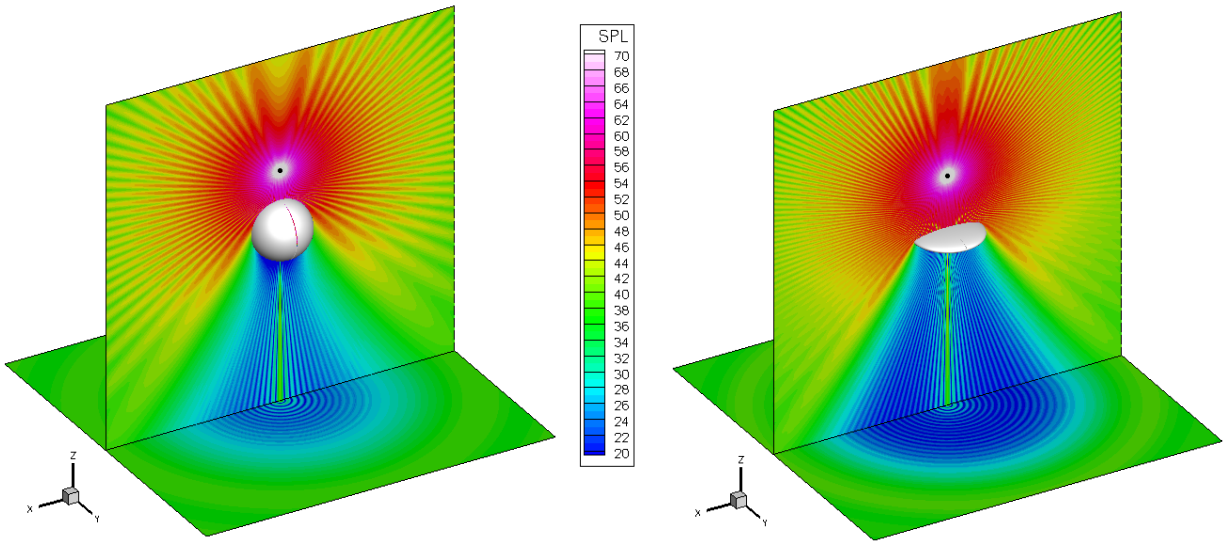

(a) Sphere (b) Oblate spheroid 1

Figure 14.- Total acoustic field, in dB, for sphere and OS1; f = 1000 Hz, M_∞ = 0.0.

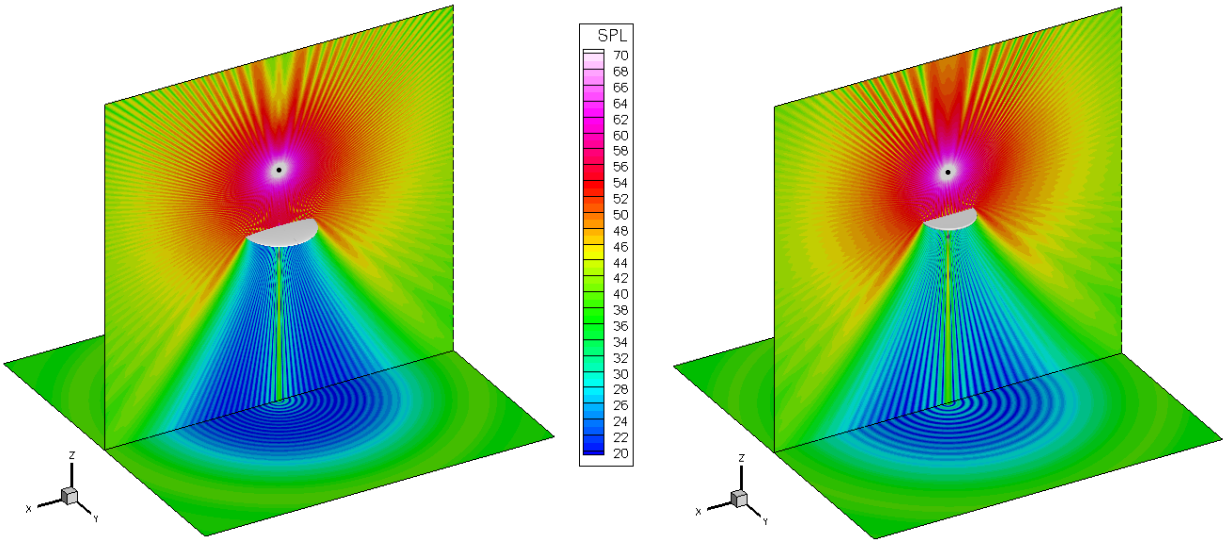

(a) Oblate spheroid 2 (b) Flat disk

Figure 15. – Total acoustic field, in dB, for OS2 and flat disk; f = 1000 Hz, M_∞ = 0.0.

A more detailed assessment of the interactions between the sound emitted by the source and the nearby surfaces can be obtained by sampling regions in the near and far acoustic fields. Sound pressure levels (SPL) in the near field – sampled at a ring with radius r = 7.5 m surrounding the scattering body (see Fig. 2a) – and in the far field – given at a line formed by the intersection of the two observer planes – are presented in Figures 16a and 16b, respectively, for an excitation frequency of 11 Hz. At this frequency, the wavelength of the sound is several times larger than the reference dimension for the surfaces (r or a). Thus, the incident field is only slightly affected by the presence of the bodies, with minor differences being caused by the geometry of the scatterers (see Fig. 16a). Plane wave propagation is almost fully established by the time the sound reaches the observing line; at this distance, scattering by any of the surfaces is negligible.

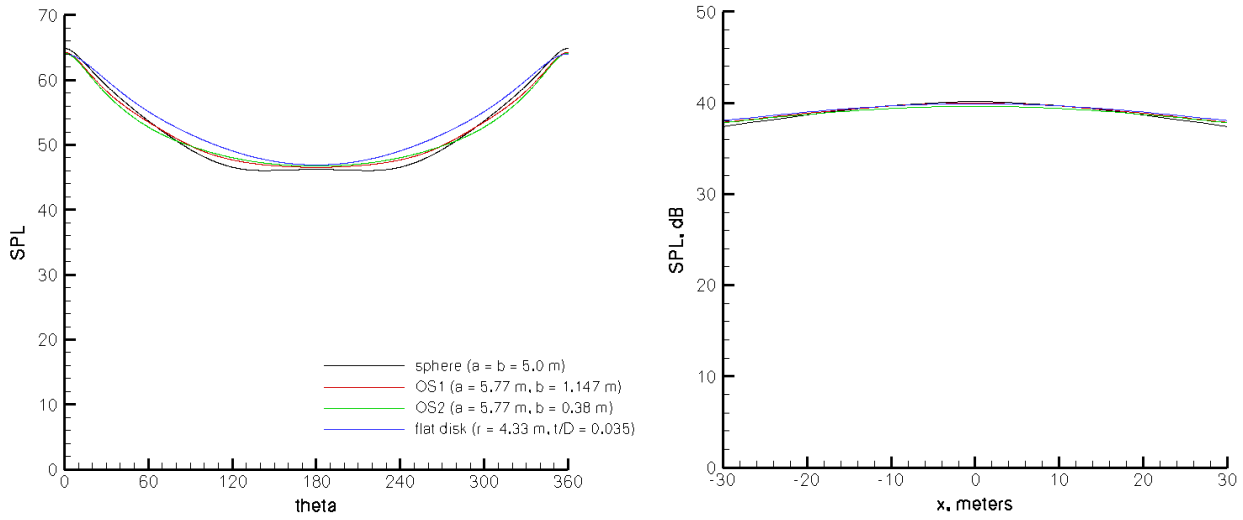

(a) Observer ring (b) Observer line

Figure 16. – Total acoustic field for oblate spheroids; f = 11 Hz (ka = 1), M_∞ = 0.0.

Observer ring and line results for f = 541 Hz are presented in Figures 17a and 17b, respectively. It is apparent from Fig. 17a that both sound amplification and shadow zones are different for all geometries considered. In the former, the interaction field for the spheroids and disk has shorter wavelength and larger amplitude than that for the sphere; the latter indicates that the spheroids, especially OS2, are more effective at attenuating sound than the sphere and disk. It can also be observed that the sphere is a slightly better noise shield than the disk in the fringes of the shadow zone (note that this may be a consequence of the relative position of the disk with respect to the observer ring). At a line 40 m from the source (Fig. 17b), the spheroids and disk have similar shielding characteristics, all better than the sphere.

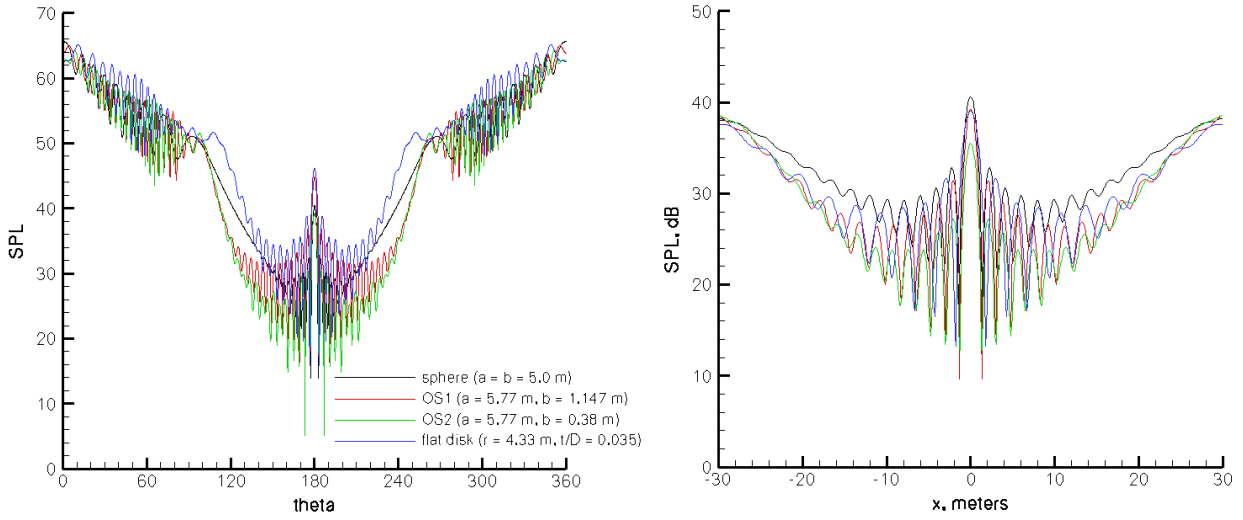

(a) Observer ring (b) Observer line

Figure 17. – Total acoustic field for oblate spheroids; f = 541 Hz (ka = 50), M_∞ = 0.0.

Similar trends can be observed at an excitation frequency f = 1000 Hz (Fig. 18), except that now OS1 has slightly better noise shielding characteristics than OS2. At f = 1623 Hz (Fig. 19), the sphere produces a larger, stronger shadow zone than the disk in the near field (Fig. 19a); in the far field, OS1 is clearly superior (Fig. 19b). These trends continue as the frequency increases (see Figures 20 – 22): OS1 has the best overall shielding characteristics; in the near field, the sphere is superior to the disk, whereas the opposite is generally noted in the far field.

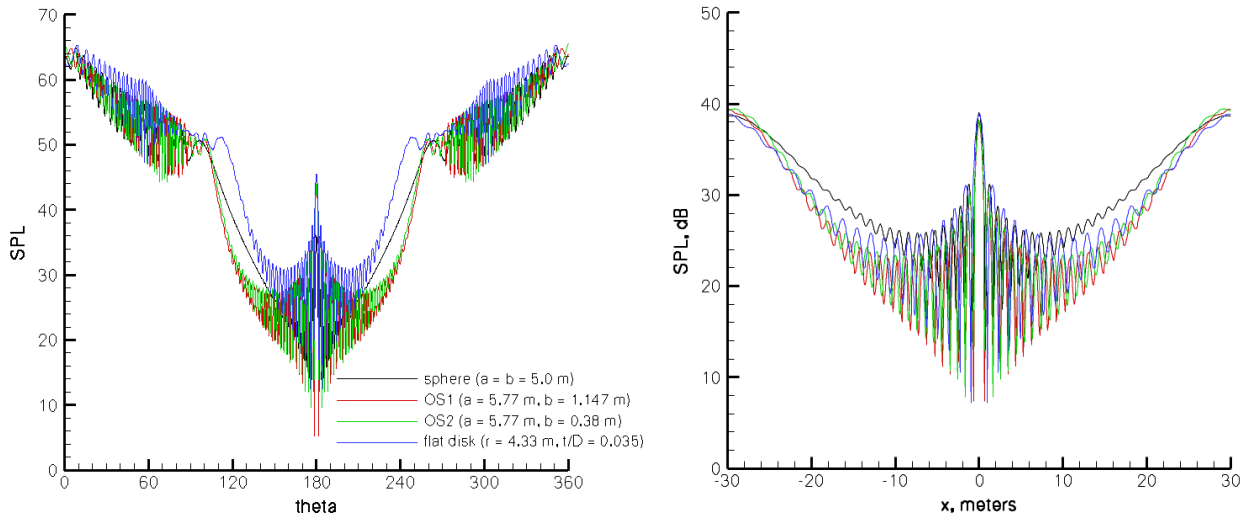

(a) Observer ring (b) Observer line

Figure 18. – Total acoustic field for oblate spheroids; f = 1000 Hz (ka = 92.4), M_∞ = 0.0.

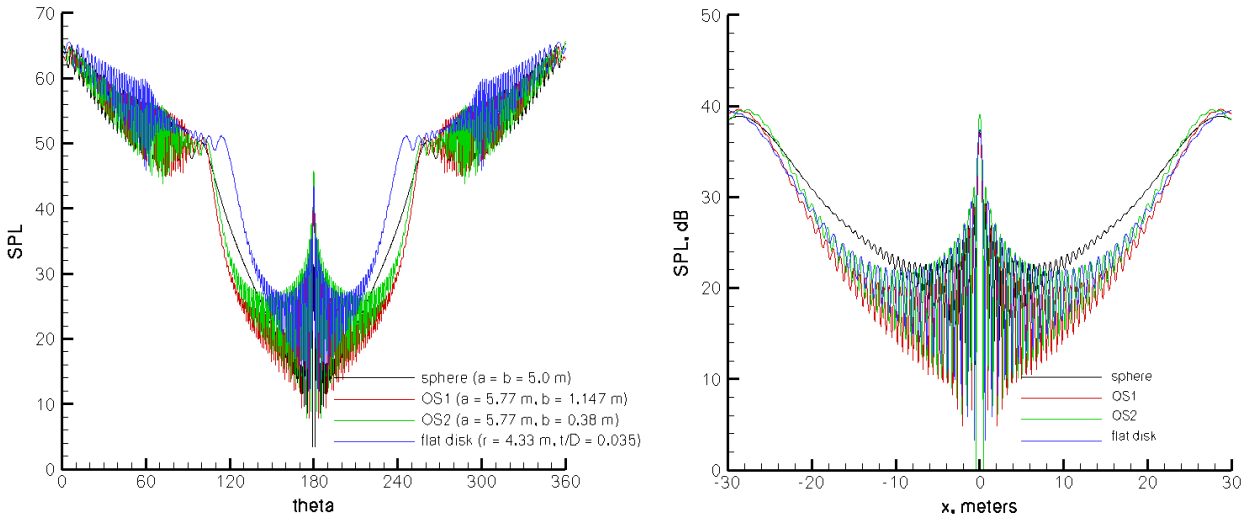

(a) Observer ring (b) Observer line

Figure 19. – Total acoustic field for oblate spheroids; f = 1623 Hz, (ka = 150), M_∞ = 0.0.

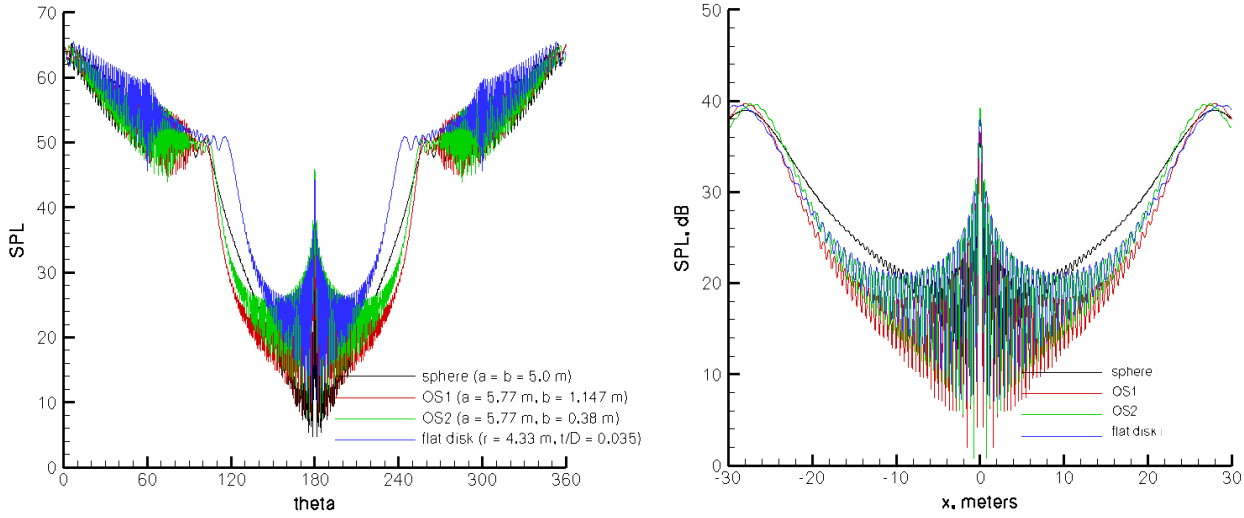

(a) Observer ring (b) Observer line

Figure 20. – Total acoustic field for oblate spheroids; f = 2164 Hz (ka = 200), M_∞ = 0.0.

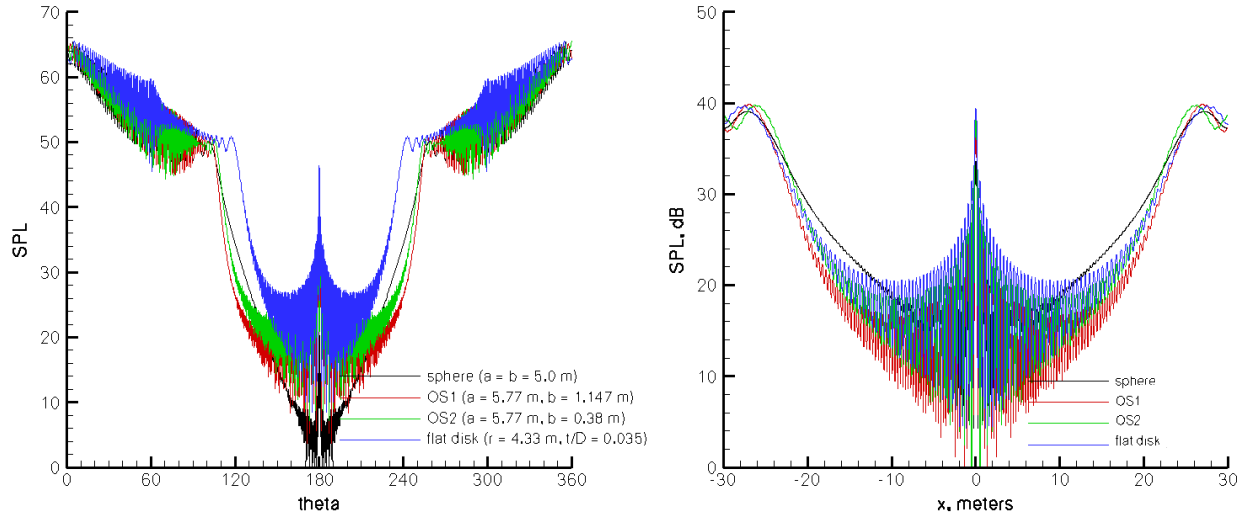

(a) Observer ring (b) Observer line

Figure 21. – Total acoustic field for oblate spheroids; f = 3247 Hz (ka = 300), M_∞ = 0.0.

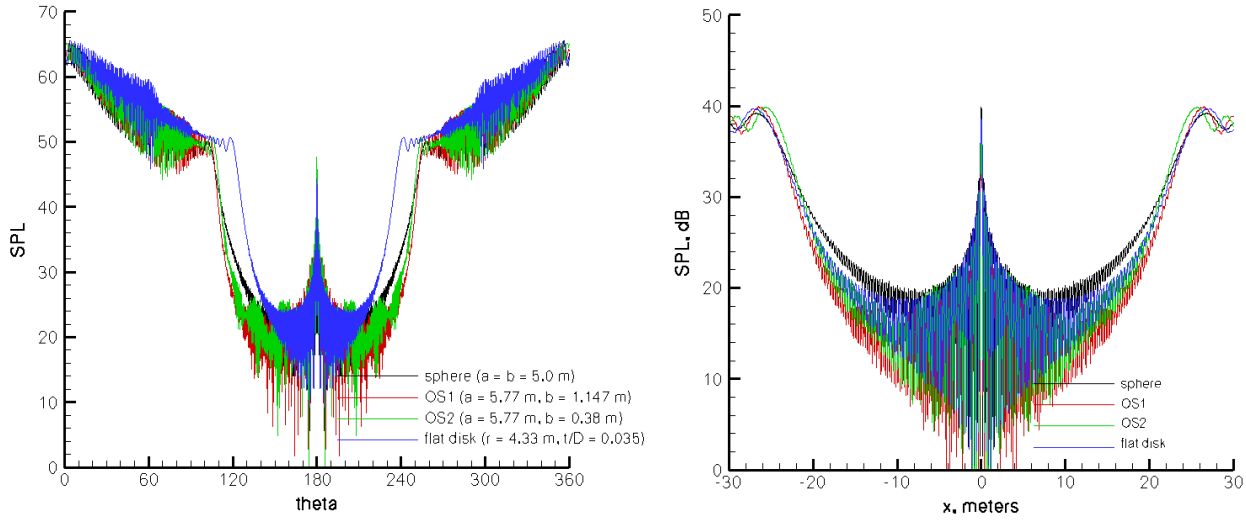

(a) Observer ring (b) Observer line

Figure 22. – Total acoustic fields for oblate spheroids; $f = 4329$ Hz ($ka = 400$), $M_\infty = 0.0$.

3.3 Flat Plate

The acoustic source used during this exercise consisted of a stationary monopole of unit strength located 0.25 m from the center of the surface; excitation frequencies were 1.0 kHz, 2.0 kHz, 4.0 kHz, and 8.0 kHz; background flow was quiescent. Grid sizes for the frequencies of interest and other metrics are provided in Table 5. Execution time statistics are given in Table 6. The total acoustic field was sampled at 1) a 2.0 m x 2.0 m plane bisecting the configuration along the plate width, and 2) a 20.0 m long line of observers located 5.0 m from the surface, opposite the sound source, traversing the width of the plate at its center.

Table 5. – Acoustic source excitation frequencies and grid metrics for flat plates.

Frequency, Hz	Square Edges		Rounded Edges		Sharp Edges	
	Grid size, (N_c x N_s)	N_w	Grid size (N_c x N_s)	N_w	Grid size (N_c x N_s)	N_w
1000	632 x 210	10.00	634 x 210	10.00	550 x 200	10.00
2000	2140 x 702	10.00	2297 x 820	10.00	1935 x 720	10.00
4000	8412 x 2808	10.00	8810 x 2926	10.00	7574 x 2508	10.00
8000	32728 x 10780	10.00	35094 x 12472	10.00	29926 x 9848	10.00

Table 6. – Execution time statistics for flat plates.

Frequency, Hz	Square Edges			Rounded Edges			Sharp Edges		
	N_{proc}	N_{iter}	t_{exec},	N_{proc}	N_{iter}	t_{exec},	N_{proc}	N_{iter}	t_{exec},
1000	4	139	3.649×10^{-3}	4	151	3.632×10^{-3}	4	153	3.117×10^{-3}
2000	4	204	3.811×10^{-2}	4	216	4.908×10^{-2}	4	290	4.722×10^{-2}
4000	8	1000	1.518	16	1000	7.432×10^{-1}	8	1000	1.126
8000	64	1600	3.987	64	1000	2.955	64	500	1.225

3.3.1 Flat Plate with Square Edges

The total acoustic field at a plane bisecting a plate with square edges is presented in Figures 23a – 23d for excitation frequencies of 1.0 kHz - 8.0 kHz. Note from the figures that 1) a well-

defined shadow zone is created by the plate, and 2) diffraction of sound by the edges increases with frequency, as manifested by "bending" of the lobes in the vicinity of the plate surface.

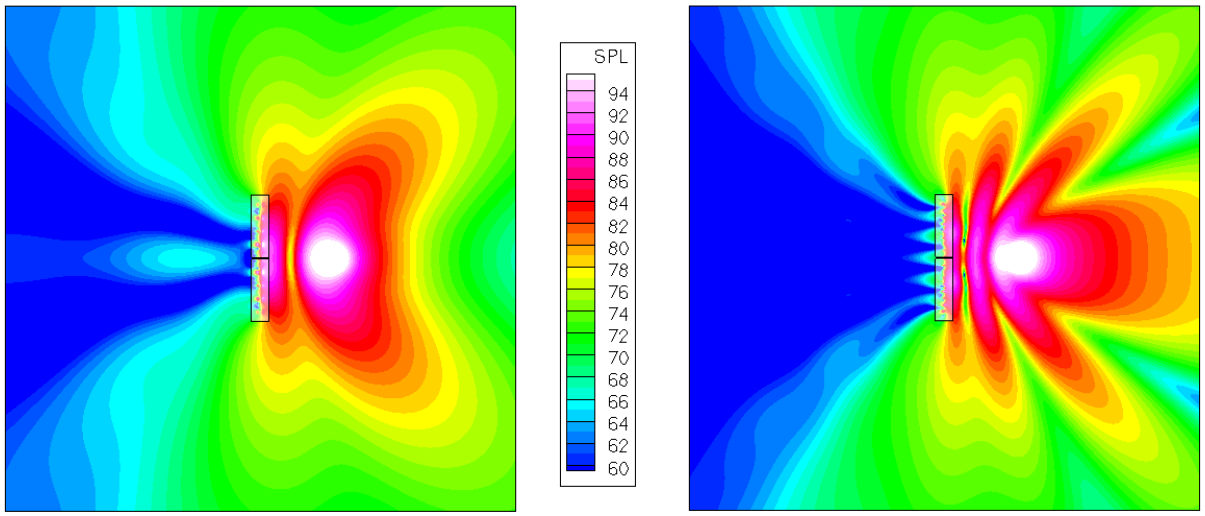

(a) f = 1000 Hz (b) f = 2000 Hz

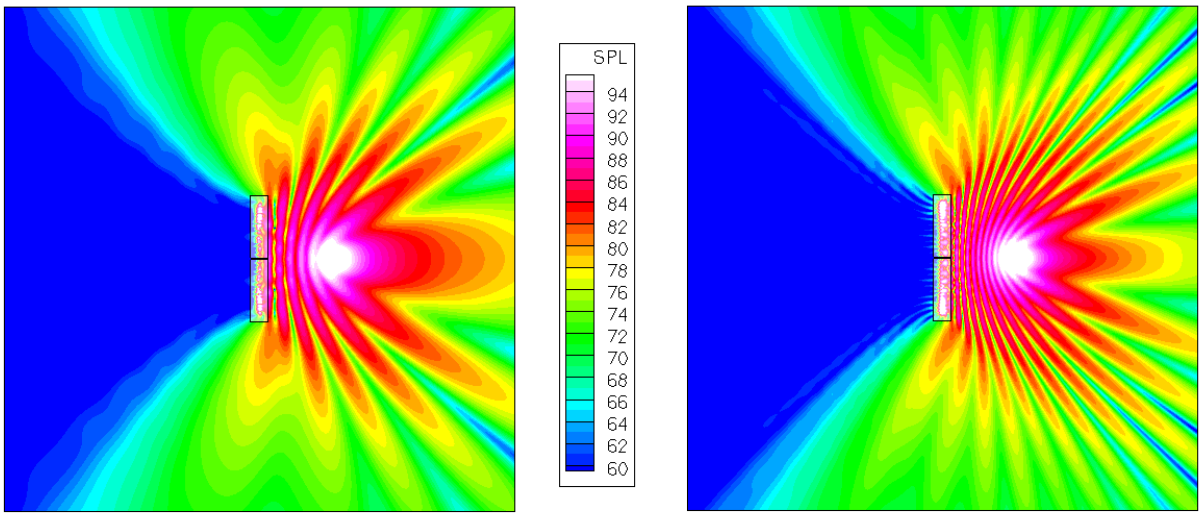

(c) f = 4000 Hz (d) f = 8000 Hz

Figure 23.- Total acoustic field, in dB, for a flat plate with square edges, M_∞ = 0.0.

The predicted total acoustic field at a line of observers crossing the shadow zone 5.0 m from the surface of the plate is compared to experimental data in Figure 24. The measurements were obtained during a series of tests described in reference 14. The data are not available in electronic form; thus, they were digitized from several figures found in the reference. As such, small inaccuracies in both amplitude and directivity are to be expected, especially at the higher frequencies. Note from Fig. 24 that the nature of the sound and its directivity are captured very well by the simulations – the peaks and valleys of the waves are generally coincident. However, the simulations tend to overpredict the benefits of shielding by 3 – 5 dB at the lower frequencies; at the highest frequency presented here (8.0 kHz), the overprediction is about 1 – 2 dB. The potential reasons for the discrepancies are numerous, notable among them:

- Limitations within the FSC methodology that prevent an accurate prediction of edge diffraction effects.
- Differences in plate thickness – The aluminum plate used in the experiment had a thickness of 0.0032 m, being almost 22 times thinner than that employed for the simulations. The close proximity of the sound source to the plate, and the low frequencies involved in the comparisons, precluded using a thin plate for the simulations. However, limited calculations using plates of different thickness (not shown) indicate that this factor may be secondary.
- Experimental difficulties related to (see ref. 14 for a detailed explanation):
  - Simulation of a purely tonal omni-directional sound source, especially at the lower frequencies.
  - Reflections from the acoustic wedges lining the anechoic chamber walls.

Despite these limitations, it is apparent that the FSC can be used to adequately predict the effects of noise shielding by a flat plate with square edges in close proximity to a point source.

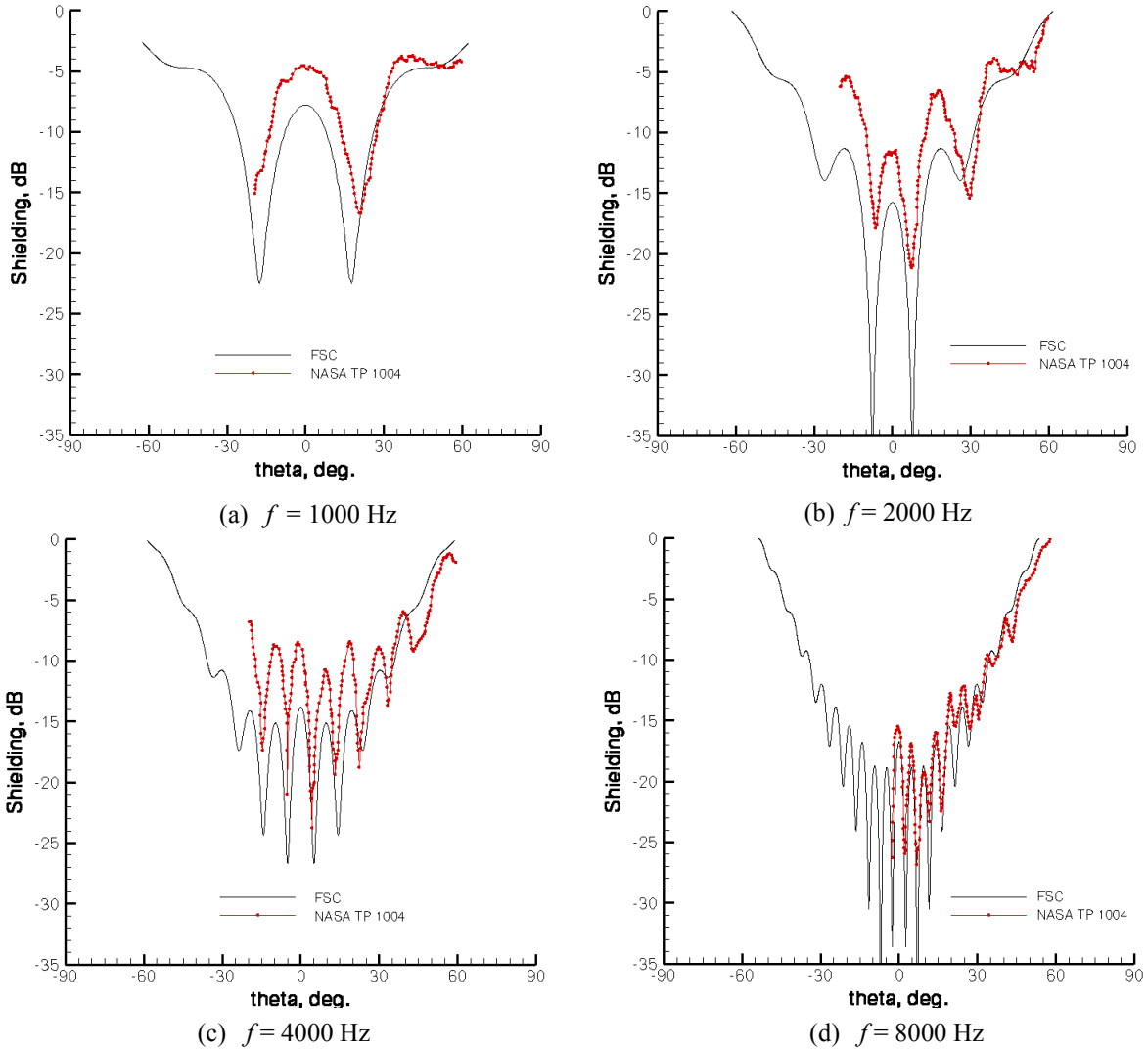

(a) f = 1000 Hz (b) f = 2000 Hz

(c) f = 4000 Hz (d) f = 8000 Hz

Figure 24.- Comparison between FSC predictions and experimental data (Figure 14 of ref. 14) for a flat plate with square edges, M_∞ = 0.0; observer line located 5.0 m from plate surface.

3.3.2 Flat Plate with Rounded Edges

The total acoustic field at a plane bisecting a plate with rounded edges is presented in Figure 25 for the excitation frequencies of interest. Although SPL contours are not discernible below 60 dB, edge diffraction effects appear to be stronger than those observed in Figs. 23a – 23d. This is to be expected, as the sound waves are better able to negotiate the gradual changes in surface slope associated with rounded edges.

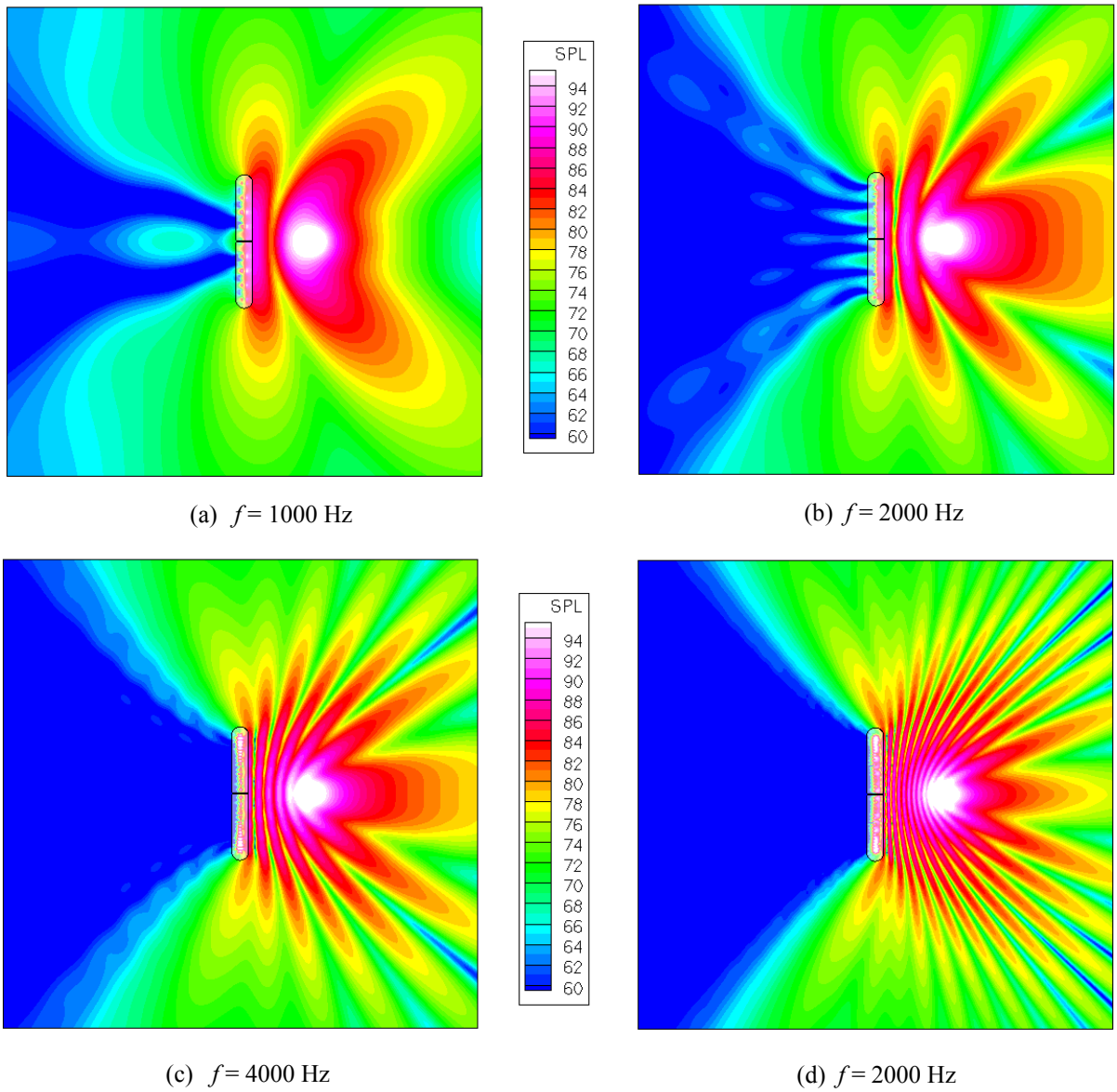

(a) f = 1000 Hz

(b) f = 2000 Hz

(c) f = 4000 Hz

(d) f = 2000 Hz

Figure 25.- Total (incident plus scattered) acoustic field, in dB, for a flat plate with rounded edges, M_∞ = 0.0.

The simulated total acoustic field at a line of observers 5.0 m from the plate surface is given in Figure 26; experimental data, available for 4.0 kHz and 8.0 kHz only, are compared to the

simulations in Figs. 26c and 26d, respectively. Note from these figures that, as before, the directivity of the sound is well matched, but the magnitude of the waves in the shadow zone is under-predicted. At these frequencies, average differences are about 5 – 6 dB. Because the plate thicknesses are comparable (0.07 m for the simulations vs. 0.051 m for the measurements), it was anticipated that the comparisons would be more favorable. A possible explanation (in addition to those mentioned in the previous section) for a portion of the discrepancies is the fact that the plate used in the experiments was made of laminated wood, which has a much higher surface roughness than that of aluminum. As a result, the reflective/diffractive behavior of the waves may have been altered, compounding the effects of edge geometry. The apparent superposition of waves in the experimental data (see Figs. 26c and 26d) could be a manifestation of this added factor.

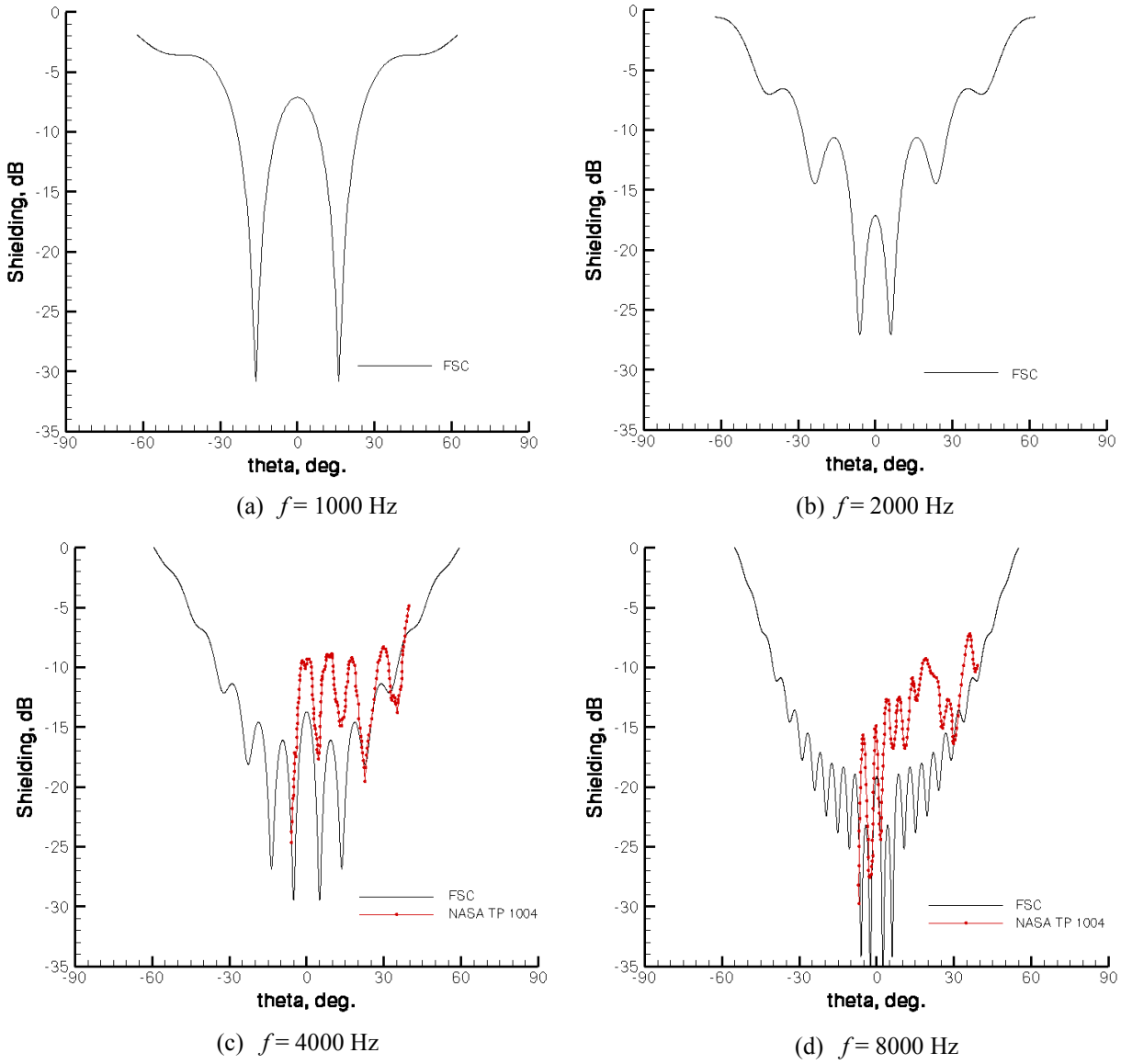

(a) $f = 1000$ Hz

(b) $f = 2000$ Hz

(c) $f = 4000$ Hz

(d) $f = 8000$ Hz

Figure 26.- Comparison between FSC predictions and experimental data (Figure 23 of ref. 14) for a flat plate with rounded edges, $M_\infty = 0.0$; observer line located 5.0 m from plate surface.

3.3.3 Flat Plate with Sharp Edges

The total acoustic field at a plane bisecting a flat plate with sharp edges is presented, as it varies with frequency, in Figures 27a – 27d. The scattered noise patterns are similar to those observed for the previous configurations: a well defined shadow zone whose demarcation increases with frequency.

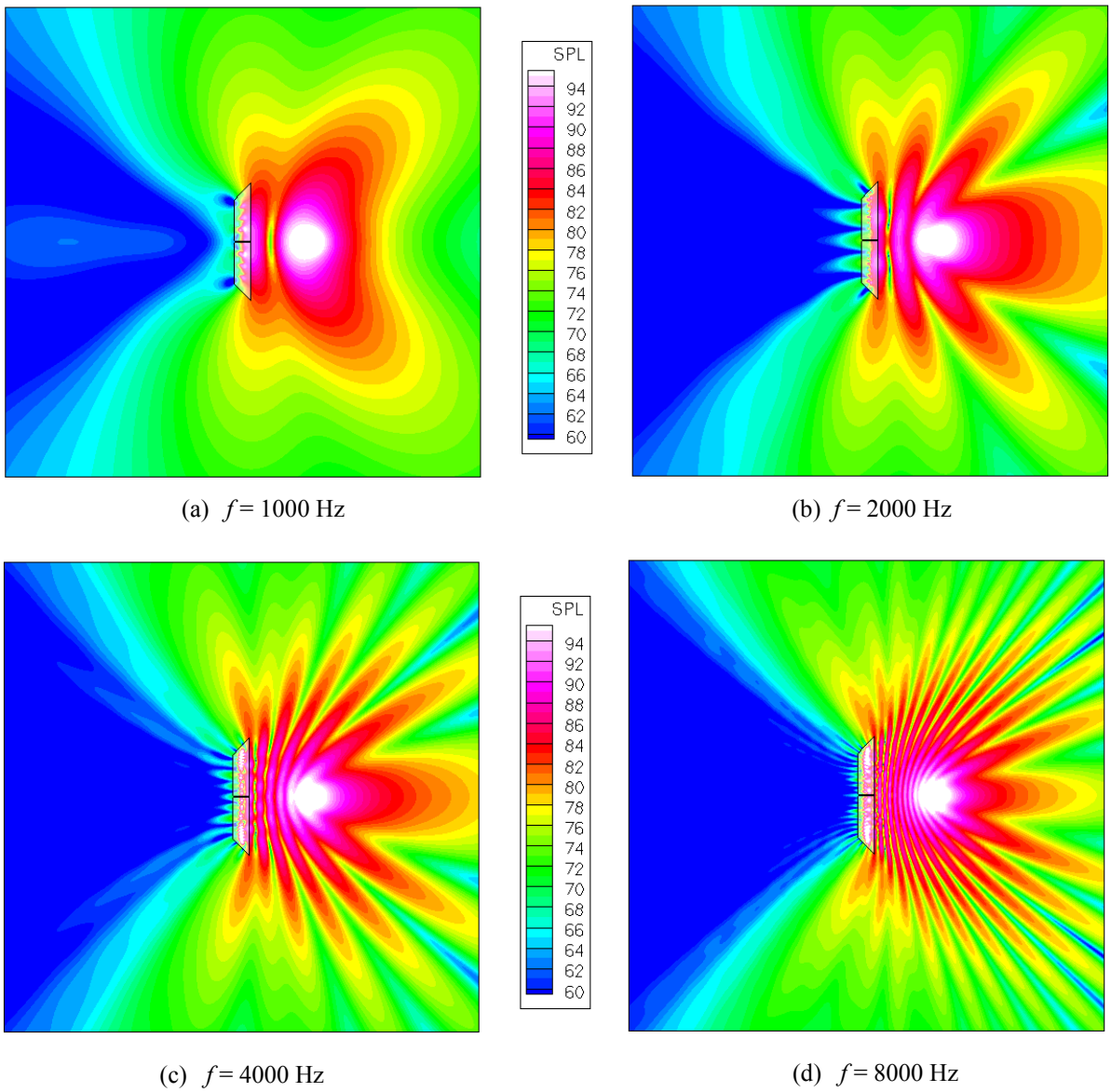

(a) $f = 1000$ Hz

(b) $f = 2000$ Hz

(c) $f = 4000$ Hz

(d) $f = 8000$ Hz

Figure 27.- Total (incident plus scattered) acoustic field, in dB, for a flat plate with sharp edges, $M_\infty = 0.0$.

The simulated acoustic field at the observer line is given in Figure 28. As was the case with the plate with rounded edges, experimental data for the lower frequencies are not available. Comparisons between predicted and measured fields are presented in Figs. 28c and 28d for 4.0 kHz and 8.0 kHz, respectively. Note from these figures that the magnitude of the waves in the

shadow zone is reasonably well predicted, the larger differences being on the order of 2 – 3 dB. Observe also that the directivity of the simulated sound agrees with that of the measurements in the central region of the shadow zone, but has an apparent phase shift toward the edges. This may be caused by the differences in plate geometry. The plate used in the experiments had a total thickness of 0.0048 m, with 0.0004 m thick sharp edges; the edges had a 20^{o} bevel. Because the plate employed in the simulations was substantially thicker, it was decided to maintain the sharpness of the edge and increase the bevel angle to about 30^{o} to avoid having sides with extensive surface area. Nevertheless, the side surface area is large enough to interact with the waves being diffracted by the sharp edge and alter their characteristics.

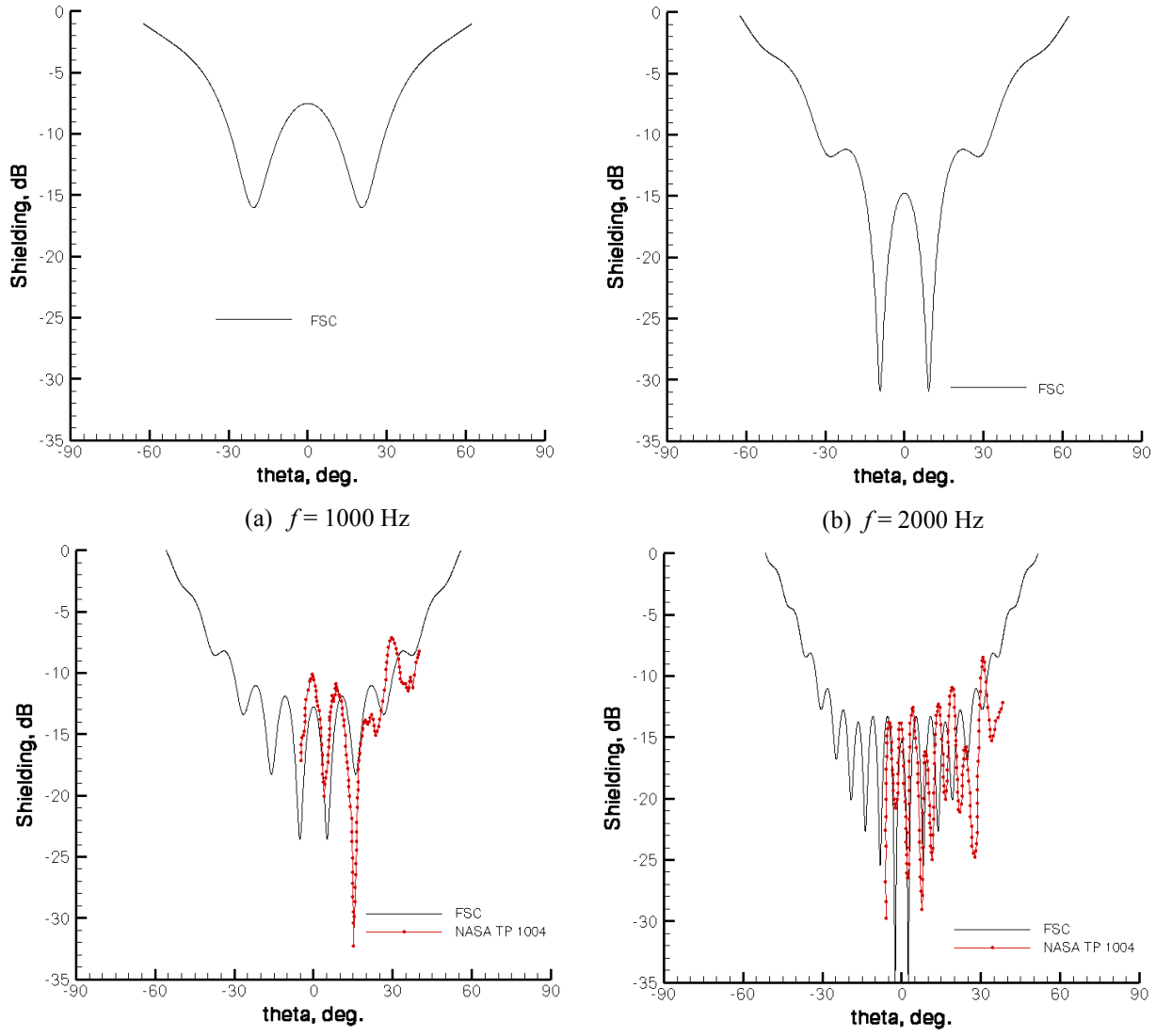

(a) $f = 1000$ Hz

(b) $f = 2000$ Hz

(c) $f = 4000$ Hz

(d) $f = 8000$ Hz

Figure 28.- Comparison between FSC predictions and experimental data (Figure 23 of ref. 14) for a flat plate with sharp edges, $M_{\infty} = 0.0$; observer line located 5.0 m from plate surface.

3.3.4 Effect of Edge Geometry on Simulated Noise Scattering

The shape of the edges may begin to affect the noise shielding characteristics of the plate when the dimensions of the edge are comparable to ¼ of the wavelength[14]. For a 0.07 m plate, edge effects may be observable at all the frequencies being considered. Simulations for the three edge types of interest are presented in Figure 29. Observe that, at the lowest frequency (Fig. 29a), variations in the magnitude of the waves toward the center of the shadow zone are very small; these differences generally increase with frequency, with the plate with rounded edges providing the most attenuation and that with sharp edges the least. Alterations in the diffraction patterns of the waves are also observable, causing a phase shift toward the edges of the shadow zone.

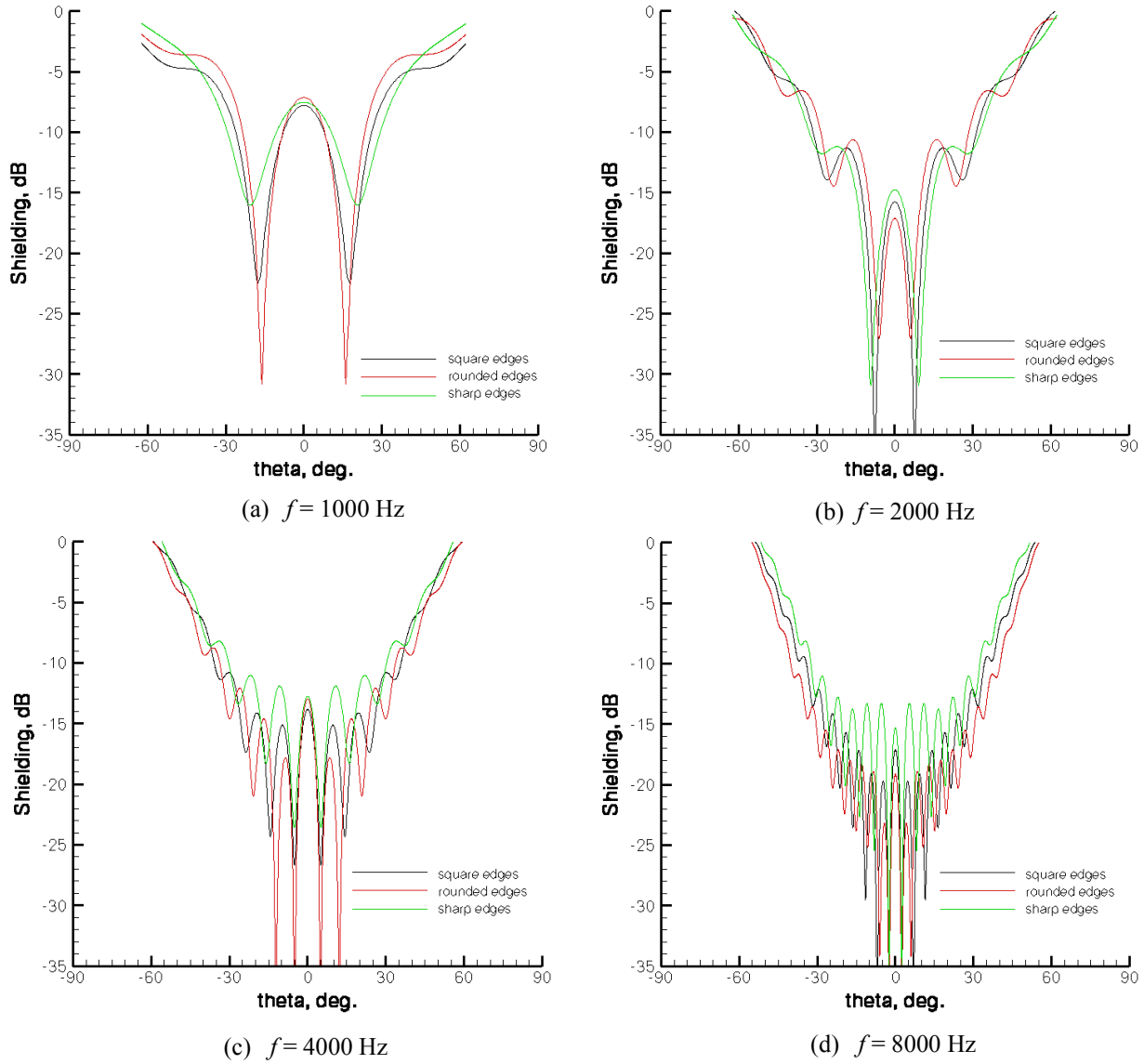

(a) $f = 1000$ Hz

(b) $f = 2000$ Hz

(c) $f = 4000$ Hz

(d) $f = 8000$ Hz

Figure 29.- Predicted effects of edge geometry on monopole noise scattering by a nearby flat plate, $M_\infty = 0.0$; observer line located 5.0 m from plate surface.

4. SUMMARY

A detailed study on the characteristics of monopole noise scattering by several simple shapes (sphere, oblong spheroids of different thickness, and a flat disk) has been conducted. The sizes of the bodies and their location with respect to the acoustic source were chosen so as to project geometrically similar shadow zones. A range of source excitation frequencies $1 \leq ka \leq 500$ was considered, and the total (incident plus scattered) acoustic field was sampled at various observer sets. The sphere simulations were compared to analytical results for validation purposes. A second study to assess the noise scattering characteristics of flat plates with different edge shapes was also performed; these simulations were compared to experimental data available in the literature. The following sections summarize the main findings of the investigation.

4.1 Sphere

- Advantage must be taken of all possible levels of symmetry within the configuration in order to obtain the correct solution and/or to improve computational efficiency.
- Surface discretization using $N_w \sim 5$ was sufficient to obtain good solutions.
- For all frequencies considered, excellent resolution of the portion of the field outside the shadow zone was obtained early in the solution process, generally within 100 – 200 iterations.
- The number of iterations required to achieve good resolution of the shadow zone increased with frequency, possibly as a result of enhanced matrix ill-conditioning due to larger numbers of equivalent sources.
- Compared to the size of the problem (N_c x N_s), convergence performance of FSC v3.1/v3.2 is excellent.
- Agreement between FSC and analytical results is remarkably good.
- Instability of the analytical approach increased with frequency; analytical solutions for the highest frequencies could not be obtained.
- Shielding effects improve with frequency – increased noise differential in the shadow zone.
- Improvements in noise attenuation due to a fully lined sphere are substantial – decreased sound amplitude and increased shielding.

4.2 Oblate Spheroids

- The relative size of the source surface should decrease with scattering body thickness in order to obtain the correct solution.
- A thin flat disk is computationally better than an oblate spheroid with similar $(t/D)_{\max}$ because of increased thickness near the edge.
- A zone of relatively high amplitude was observed in the shadow zone opposite to the source. This behavior is intrinsic to the governing equations.
- The best overall performer was OS1.
- In the near field, the sphere was more effective than the disk; in the far field, the opposite was true.
- In general, shielding effects increase with frequency for all configurations.

4.3 Flat Plate

Comparison with experimental data at several frequencies in the low to mid range indicates that the FSC is capable of predicting the correct characteristics and trends of the wave interaction patterns in the shadow zone, especially at higher frequencies.

5. GUIDELINES FOR SUCCESSFUL APPLICATION OF THE FSC TO GENERAL SCATTERING PROBLEMS

There is little guidance in the literature regarding the type and number of source points to be used for ESM simulations, their distribution on the source surface, and the location of such a surface relative to the scattering body. Extensive numerical experimentation has been performed to establish general rules of thumb for using the FSC to solve an arbitrary scattering problem. The following sections summarize the lessons learned by the authors during the performance of a wide range of scattering simulations, including the present investigation. Where appropriate, reference is made to specific portions of the User's Manual (ref. 2) to supplement the information provided here.

5.1 Solution Quality

The quality of a solution is affected by several factors: scattering surface definition (shape and size of the body), scattering surface discretization (number and distribution of collocation points), source surface discretization (type, number, and distribution of equivalent sources), placement of the source surface inside the scatterer, and configuration symmetry.

5.1.1 Scattering Surface Definition

The user is responsible for providing a surface definition that is compatible with FSC requirements (see section 2.3.1.2 of ref. 2). The input surface grid should 1) be dense enough for an accurate definition of the surface of interest; and 2) have uniform spacing, as the surface discretization process follows grid topology.

5.1.2 Scattering Surface Discretization

The geometry module of the FSC produces a uniform[§] distribution of collocation points on the scattering surface. The number of collocation points (N_c) is proportional to Sk^2, where S is surface area and k is wave number (see section 1.4.1 of ref. 2). The proportionality factor depends on a user selected number of points per wavelength (N_w) and on flow speed. The choice of N_w is frequency dependent; a suitable range is $5 < N_w < 12$. For higher frequencies, use lower values ($N_w \sim 5$, or even lower, works well); for lower frequencies, user higher values (see section 2.3.1.6 of ref. 2). For very low frequencies, when the wavelength is larger than the reference dimension of the surface, much larger values ($N_w \sim 50$) should be used.

5.1.3 Source Surface Discretization

The geometry module generates a uniform distribution of equivalent sources on the source surface. The types of equivalent sources that can be used with FSC v2.0 are monopoles

[§] It has been determined that a uniform distribution of collocation points and equivalent sources is necessary to minimize matrix ill-conditioning.

(stationary or spinning) and dipoles. Only stationary monopoles can be used with FSC v3.1/3.2; however, they are very well suited for the vast majority of applications. For exterior BVPs, the number of equivalent sources (N_s) should be about $1/3N_c$ (see section 2.3.1.6 of ref. 2). For interior BVPs, the ratio can be slightly smaller: for room acoustics, $N_s = 0.3N_c$ works well; for modal noise propagation within ducts, $N_s \sim 0.15N_c$ is a good choice.

5.1.4 Source Surface Placement

The FSC generates source surfaces by creating smaller versions of the scatterers based on a single user supplied scaling parameter (*srcalph*). To ensure that the source surface is interior to the scattering body (a requirement of the ESM for exterior BVPs), it is anchored at the leading and trailing edges for wing-like structures, and at the nose and tip for fuselage-like structures. The size and shape of the resulting source surface can substantially affect the quality of a solution.

5.1.4.1 Source surface size

An adequate source surface size (relative to the scattering surface) depends on 1) the excitation frequency of the incident sound, 2) the shape/surface area of the scatterer (see section 2.3.1.5 of ref. 2), and 3) the distance between the scatterer and the acoustic source. In general, for moderate to high frequencies and relatively large, thick bodies, *srcalph* ~ 0.9 to 0.95 gives excellent results; the thinner the surface, the lower the frequency, and/or the closer the acoustic source is to the surface, the smaller *srcalph* should be. For example, *srcalph* ~ 0.75 to 0.8 works well for nacelles at most frequencies of interest; for very thin bodies (thickness ratio of about 0.03 to 0.05), *srcalph* can be as low as 0.1.

5.1.4.2 Source surface shape

A constant separation between source and scattering surfaces is desirable; this cannot be maintained in the regions where the source surface is anchored to the scattering body. Most geometries of interest are composed of wing-like structures and/or fuselages; for these, the effects of non-constant separation at the edges are small. For canonical shapes like spheres, cylinders, and cubes, the effect is more pronounced. In these cases, the geometry module can still be used advantageously by using separate, properly constructed scattering and source surfaces as inputs (see section 2.3.1.1 of this report).

5.1.5 Use of Symmetry

As indicated in section 2.1.1 of the present report, the ESM is susceptible to matrix ill-conditioning for highly symmetric configurations. To avoid potential problems, advantage must be taken of all degrees of symmetry available in the configuration/system. An added benefit of doing so is a substantial reduction in matrix size, as only a portion of the scattering body of interest needs to be considered. Thus, for a given computer system, the savings in execution time permits consideration of higher excitation frequencies.

5.2 Solution Accuracy/Convergence

The accuracy of a solution obtained with the FSC can be assessed in a variety of ways. The obvious first choice is to compare FSC results to those obtained from analytical approximations;

however, such expressions do not exist for realistic problems involving bodies of arbitrary shape. For these, the following three tests should be performed; if their outcome is satisfactory, the user can be confident that the solution is accurate.

5.2.1 Sound through Solid Surfaces

A simple test to qualitatively determine the correctness of a solution is to sample the total acoustic field at a plane bisecting the configuration to determine if 1) sound appears to be going through the scattering surfaces, and 2) a well defined shadow zone is present. Consider, for example, the system composed of a thin oblate spheroid and a monopole source located 7.5 m from the surface presented in Figure 30. The source excitation frequency is 1000 Hz, no background flow. Fig. 30a corresponds to a solution obtained with a 90% equivalent source surface size. Note from the figure that sound seems to be penetrating the solid surfaces, and that a shadow zone – which should be clearly present at this frequency – is missing. This behavior is evidence that the relative distance between the scattering and source surfaces is too small. Reducing the scale of the source surface to 60% (Fig. 30b) and 20% (Fig. 30c) noticeably improved the shielding characteristics of the thin spheroid. Although not shown here, additional decrements in source surface size did not appreciably change the scattering patterns. Further improvements could only be obtained by increasing the thickness of the scattering body, as shown in Fig. 30d.

The process described above was continued until an "optimum" combination of scattering surface thickness and source surface size was achieved, resulting in the observation that a thin flat disk with a rounded edge is numerically more efficient than an oblate spheroid with similar dimensions (see section 2.3.1.1). The total acoustic field for this thin flat disk at a plane bisecting the system is presented in Figure 31. Determination of a suitable source surface size using this approach can be tedious; however, the authors have observed that once found, the same source surface can be used for a wide range of acoustic source excitation frequencies.

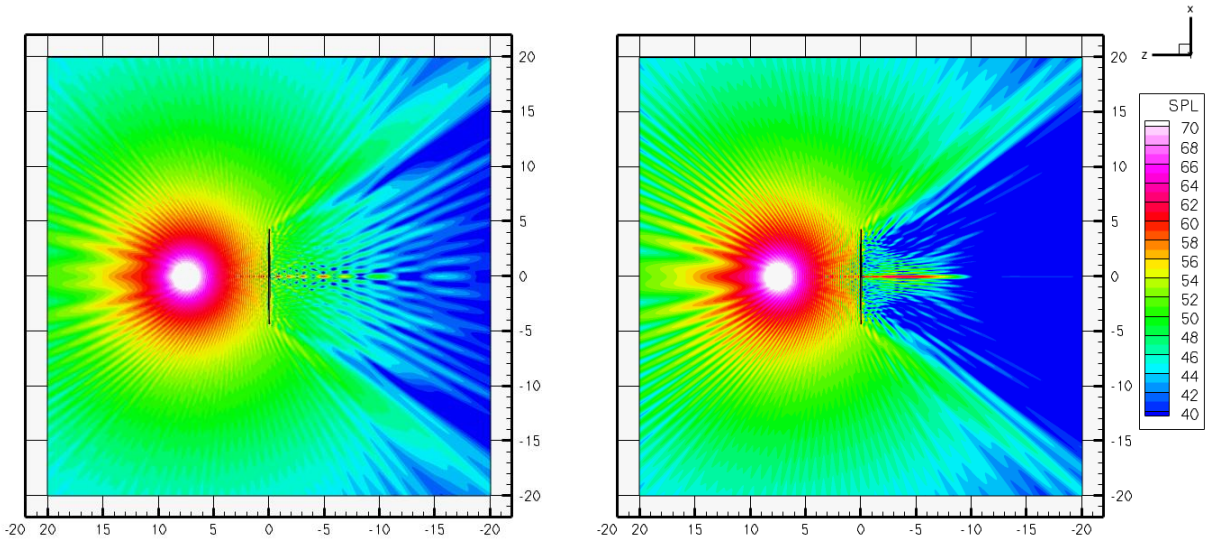

(a) $b = 0.1$ m, *srcalpha* = 0.9

(b) $b = 0.1$ m, *srcalpha* = 0.6

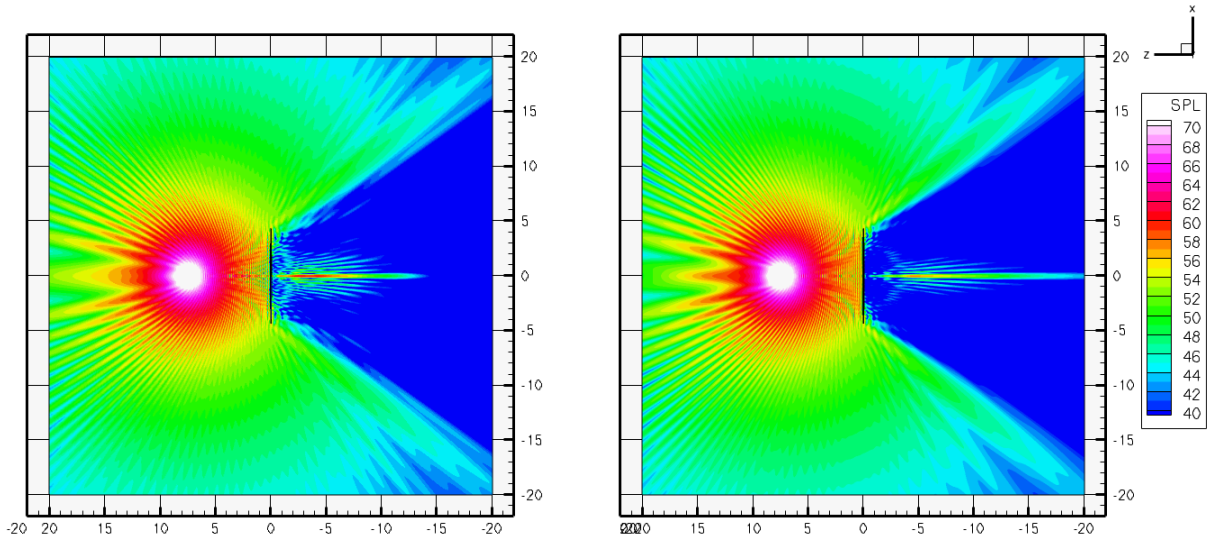

(c) $b = 0.1$ m, *srcalpha* = 0.2 (d) $b = 0.125$ m, *srcalpha* = 0.2

Figure 30. – Total acoustic field (in dB) on a plane bisecting a thin oblate spheroid ($a = 4.33$ m), $f = 1000$ Hz, $M_\infty = 0.0$.

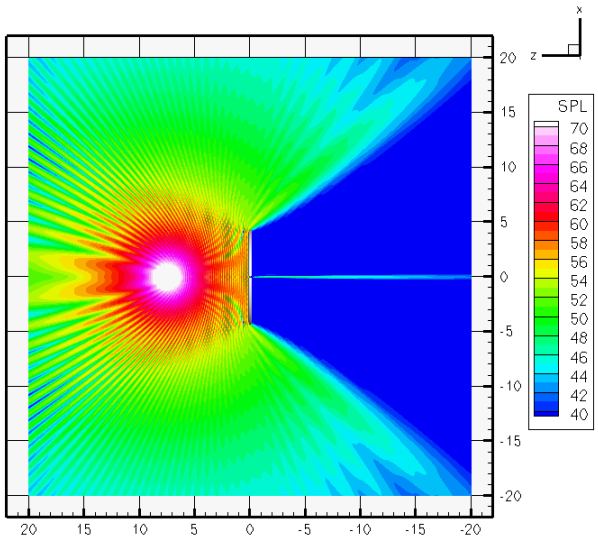

Figure 31. – Total acoustic field (in dB) on a plane bisecting a thin flat disk with rounded edges ($r = 4.33$ m, $t/D = 0.035$), $f = 1000$ Hz, $M_\infty = 0.0$.

5.2.2 Convergence Metrics

The FSC outputs iteration convergence histories for three metrics: the normalized L2 norms of the solution (source strength) vector residual, the square root of the solution vector, and the residual vector (see section 1.2.1.3 of the FSC v3.1/3.2 user's manual, ref. 15). The first metric gives an indication of solution convergence; the last follows the magnitude of the boundary condition residual at the scattering surfaces. Figures 4b - 11b depict the convergence history for the first and third metrics, as obtained during the sphere scattering exercise. Final values for

these two parameters are given in Table 6 for the oblate spheroids. Similar information is provided in Table 7 for the flat plate with square edges.

Table 7. – Final values of normalized L2 norms for oblate spheroids.

***f*, Hz**	***ka***	**Sphere**		**OS1**		**OS2**		**Flat Disk**	
		Solution vector	**BC error**	**Solution vector**	**BC error**	**Solution vector**	**BC error**	**Solution vector**	**BC error**
11	1.0	7.65×10^{-8}	4.99×10^{-3}	5.07×10^{-6}	1.00×10^{-2}	5.13×10^{-6}	1.61×10^{-3}	1.15×10^{-7}	1.49×10^{-4}
541	50.0	9.91×10^{-7}	4.62×10^{-5}	6.59×10^{-6}	5.65×10^{-4}	5.08×10^{-6}	5.63×10^{-4}	4.71×10^{-6}	2.61×10^{-4}
1000	92.4	9.55×10^{-6}	4.38×10^{-6}	3.19×10^{-7}	3.55×10^{-4}	7.99×10^{-6}	5.08×10^{-4}	5.69×10^{-6}	1.85×10^{-4}
1623	150.0	7.36×10^{-6}	3.77×10^{-6}	9.64×10^{-6}	4.15×10^{-5}	9.81×10^{-6}	2.01×10^{-4}	1.28×10^{-4}	3.10×10^{-4}
2164	200.0	4.17×10^{-5}	2.79×10^{-6}	9.80×10^{-6}	2.96×10^{-5}	1.79×10^{-5}	5.35×10^{-3}	6.37×10^{-4}	2.79×10^{-4}
3247	300.0	3.52×10^{-5}	8.16×10^{-6}	3.86×10^{-4}	1.77×10^{-4}	5.78×10^{-4}	6.40×10^{-4}	5.52×10^{-4}	3.52×10^{-4}
4329	400.0	2.74×10^{-4}	9.59×10^{-5}	6.86×10^{-4}	5.89×10^{-3}	1.87×10^{-3}	2.09×10^{-2}	1.10×10^{-3}	1.90×10^{-2}
5411	500.0	9.56×10^{-4}	2.43×10^{-3}						

Table 8. – Final values of normalized L2 norms for flat plate with square edges.

Frequency, Hz	**Solution vector**	**BC error**
1000	8.24×10^{-6}	1.88×10^{-3}
2000	7.75×10^{-6}	5.22×10^{-3}
4000	7.03×10^{-4}	3.11×10^{-2}
8000	3.68×10^{-4}	2.28×10^{-3}

5.2.3 Acoustic Power through a Sphere

The average rate of acoustic energy radiation from a source is known as sound power. Because it is spatially and temporally independent, acoustic power can be used to measure the losses in a system. For sound scattering simulations using the ESM, the changes in radiated energy may result from physical reasons such as the inclusion of sound absorbing material on the surfaces[3], or from numerical inaccuracies caused by an improper definition/placement of the equivalent sources.

A convenient way to test the correctness of the ESM setup for acoustically hard surfaces is to calculate the sound power through a sphere of arbitrary radius surrounding the configuration[16]. The scattering of sound by untreated surfaces is a non-dissipative process; thus, the incident acoustic power on the sphere surface should be the same as the total (incident plus scattered) power. All versions of the FSC include intensity/power calculations for the sphere observer field (*iobs* = 2). Consider, for example, the monopole/thin flat disk system introduced in section 2.3.1, and depicted in Figure 32 as surrounded by a closed sphere of radius 10 m centered at the source. The incident power flowing through the sphere is 3.837×10^{-4} W (PWL = 85.84 dB), the total power is 3.863×10^{-4} W (PWL = 85.87 dB). The error in PWL is thus 0.035%.

The outcome from the present test, and from those described in sections 5.2.1 and 5.2.2, indicate that the solution obtained with the FSC for the scattering of monopole sound (f = 100 Hz, M_∞ = 0.0) by a thin flat disk is highly accurate.

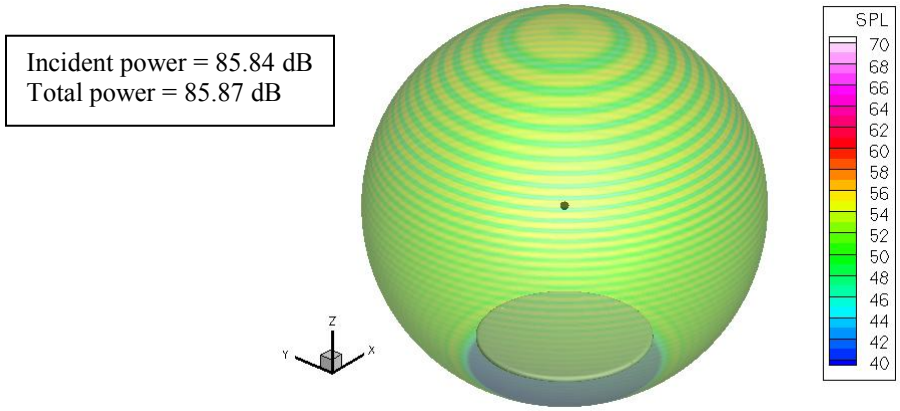

Figure 32. – Total acoustic field, in dB, on a sphere (r = 10 m) surrounding the thin flat disk /monopole system, f = 1000 Hz, M_∞ = 0.0. The sphere is centered at the source.

5.3 Grid Density Effects on Solution Accuracy

As can be observed from Tables 2 and 4, the computer resources necessary to achieve convergence can be prohibitive for high frequency/large scale scattering simulations. Previous investigations by the authors[6] suggest that the nominal density (size) of an FSC matrix can be decreased substantially for higher excitation frequencies without compromising the accuracy of a solution; the reduction factor appeared to increase with frequency. For a given excitation frequency, the geometry module can be used to generate FSC grids of any size by adjusting N_w (see section 5.1.2).

5.4 Application to Partial Configurations

For a given configuration, the computational time required to solve scattering problems increases substantially with frequency. However, in certain instances, components of interest can be isolated without significant loss of accuracy. This can be very useful when performing parametric analyses, since execution times are substantially reduced. Results from an exercise conducted for a full scale commercial transport (wings, fuselage and sideboard nacelle) similar in size and shape to the Boeing 777 are presented in Figure 33. The incident sound was generated by the lowest cut-on circumferential mode of rotor-stator interaction tones (m = 10) for an engine/nacelle configuration similar to the GE-90; the source excitation frequency was f = 2 x BPF (fan), M_∞ = 0.2 (uniform). Surface insertion loss** contours calculated using the entire configuration are depicted in Fig. 33a in the vicinity of the wing/nacelle area. The fuselage was then removed from the configuration and a new acoustic field was obtained; this field is presented in Fig. 33b, for the same wing/nacelle region as before. Note that the differences between the two approaches are small, and confined mainly to the wing/fuselage junction, as expected.

** Insertion loss was calculated by subtracting the nacelle alone contributions from the fuselage/wing/nacelle data. Negative values mean a reduction in noise; positive values indicate a gain.

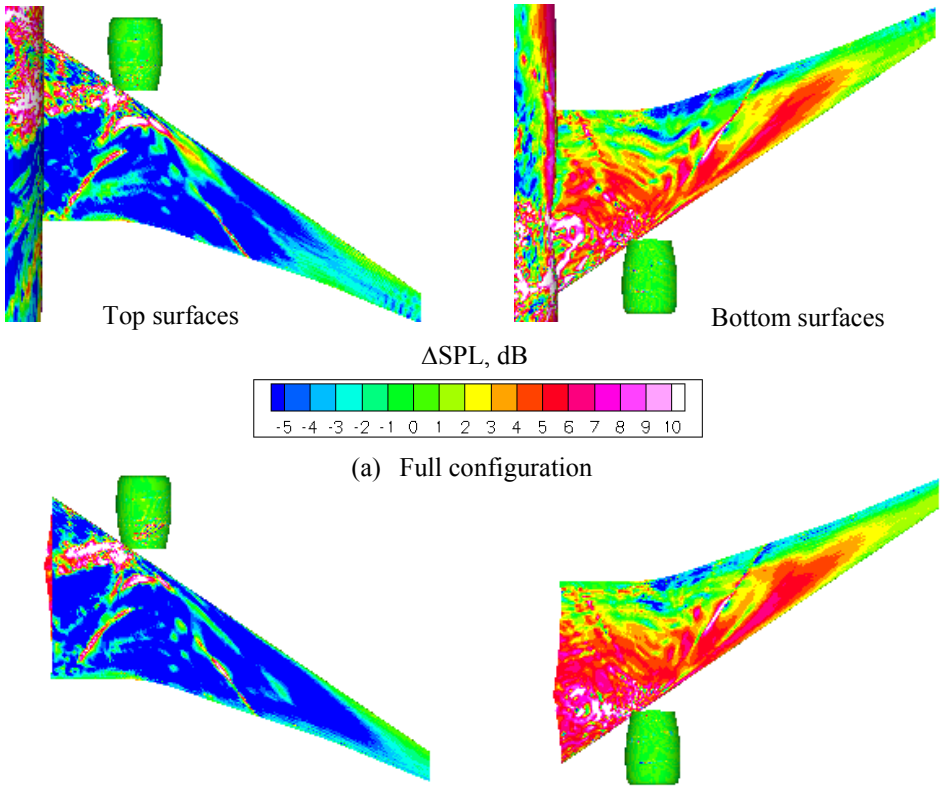

(a) Full configuration

(b) Wing plus nacelle only

Figure 33. Insertion loss for full scale transport component isolation. Incident sound is lowest cut-on circumferential mode of rotor/stator interaction; f = 2 x BPF (fan), M_∞ = 0.2.

5.5 Problem Setup – A Roadmap

Successful application of the FSC to arbitrary scattering problems requires that the user be familiar with the code, its workings, and the methodology behind it. The user's manuals[2,15] have been written for this purpose. They contain detailed explanations of the various input/output parameters and options, as well as several sample cases to guide the learning process.

The procedure for obtaining an adequate solution with the FSC is the same for all configurations. Assuming that the input surfaces are properly defined (see section 5.1.1 of this report), the following checks should be performed using the visualization files produced by the geometry module (section 2.3.1.4, ref. 2):

a) Spline-fitted shapes for the scattering and source surfaces are as expected (section 2.3.1.7 of ref. 2).

b) Collocation points and equivalent sources are uniformly distributed.

c) Surface normal vectors at the collocation points and equivalent sources are pointing in the correct direction (outward for exterior BVPs, inward for interior BVPs. The geometry module only supports the former).

If everything checks, the user can be confident that the collocation point and equivalent source files contain the correct information. Input these files into the ESM module:

a) Run the code for a few hundred iterations (more for low frequencies, less for high frequencies).

b) Check the residual history file to determine if the solution is converging. For well-conditioned problems, convergence is fast; for ill-conditioned problems, convergence may be slow.

c) Calculate the acoustic field at a plane bisecting the configuration, including the incident sound source:

- Make sure the incident field is as expected.
- Examine the total acoustic field. If sound appears to be going through the scattering surfaces, and/or an expected shadow zone is not discernible, then
  - The size of the source surface may need to be adjusted (most likely).
  - More iterations are required.

d) Go back to (a) and repeat the process until the desired convergence/behavior is achieved.

e) Calculate the acoustic field at other desired observer locations.

6. REFERENCES

1. Dunn, M. H., and Tinetti, A. F., "Aeroacoustic Scattering Via the Equivalent Source Method," AIAA 2004-2937, May 2004.
2. Tinetti, A, F., Dunn, M. H., and Pope, S. D., "Fast Scattering Code (FSC) User's Manual, Version 2.0," NASA CR 2006-214510, October 2006.
3. Reimann, C. R., Tinetti, A. F., and Dunn, M. H., "Engine Liner Optimization Using the Fast Scattering Code," AIAA 2007-3494, May 2007.
4. Lee, S., Erwin, J., and Brentner, K., "Acoustic Scattering of Rotorcraft Noise," AHS 64th annual forum, April 2008.
5. Gerhold, C. H., Clark, L. R., Dunn, M. H., and Tweed, J., "Investigation of acoustical shielding by a wedge-shaped airframe," *Journal of Sound and Vibration*, Vol. 294, pp. 49-63, 2006.
6. Tinetti, A. F., and Dunn, M. H, "Scattering of High Frequency Duct Noise by Full Scale Hybrid Wing Body Configurations," AIAA 2009-3400, May 2009.
7. Posey, J. W., Tinetti, A. F., and Dunn, M. H., "The Low-Noise Potential of Distributed Propulsion on a Catamaran Aircraft," AIAA 2006-2622, May 2006.
8. Farassat, F., Casper, J. H., Tinetti, A. F., and Dunn, M. H., "Airframe Noise Prediction by Acoustic Analogy: Revisited," AIAA 2006-2564, May 2006.
9. Tinetti, A. F., and Dunn, M. H., "Acoustic Simulations of an Installed Tandem Cylinder Configuration," AIAA 2009-3158, May 2009.
10. Dunn, M. H., and Tinetti, A. F., "Application of Fast Multipole Methods to the NASA Fast Scattering Code," AIAA 2008-2875, May 2008.
11. Ochmann, M., "The Source Simulation Technique for Acoustic Radiation Problems", *Acustica*, Vol. 81, pp. 512 – 627, 1995.

12. Gumerov, N. A., and Duraiswami, R., Fast Multipole Methods for the Helmholtz Equation in Three Dimensions, Elsevier Series in Electromagnetism, 2004.
13. Zhang, S., and Jin, J., Computation of Special Functions, John Wiley & Sons, Inc., 1996.
14. Ahtye, W. F., and McCulley, G., "Evaluation of Approximate Methods for the Prediction of Noise Shielding by Airframe Components," NASA TP 1004, January 1980.
15. Tinetti, A. F., and Dunn, M. H., "FSC versions 3.1 and 3.2," addendum to the FSC v2.0 manual.
16. Lee, S., Brentner, K., and Morris, P., "Assessment of Time-Domain Equivalent Source Method for Acoustic Scattering," AIAA 2010-3821, May 2010.

REPORT DOCUMENTATION PAGE

Form Approved
OMB No. 0704-0188

1. REPORT DATE *(DD-MM-YYYY)*	2. REPORT TYPE	3. DATES COVERED *(From - To)*
01- 06 - 2011	Contractor Report	

4. TITLE AND SUBTITLE

The Fast Scattering Code (FSC): Validation Studies and Program Guidelines

5a. CONTRACT NUMBER

NNL09AA17C

5b. GRANT NUMBER

5c. PROGRAM ELEMENT NUMBER

6. AUTHOR(S)

Tinetti, Ana F.; Dunn, Mark H.

5d. PROJECT NUMBER

5e. TASK NUMBER

5f. WORK UNIT NUMBER

561581.02.08.07.18.14

7. PERFORMING ORGANIZATION NAME(S) AND ADDRESS(ES)

NASA Langley Research Center
Hampton, VA 23681-2199

8. PERFORMING ORGANIZATION REPORT NUMBER

9. SPONSORING/MONITORING AGENCY NAME(S) AND ADDRESS(ES)

National Aeronautics and Space Administration
Washington, DC 20546-0001

10. SPONSOR/MONITOR'S ACRONYM(S)

NASA

11. SPONSOR/MONITOR'S REPORT NUMBER(S)

NASA/CR-2011-217158

12. DISTRIBUTION/AVAILABILITY STATEMENT

Unclassified - Unlimited
Subject Category 71
Availability: NASA CASI (443) 757-5802

13. SUPPLEMENTARY NOTES

Langley Technical Monitor: Douglas M. Nark

14. ABSTRACT

The Fast Scattering Code (FSC) is a frequency domain noise prediction program developed at the NASA Langley Research Center (LaRC) to simulate the acoustic field produced by the interaction of known, time harmonic incident sound with bodies of arbitrary shape and surface impedance immersed in a potential flow. The code uses the equivalent source method (ESM) to solve an exterior 3-D Helmholtz boundary value problem (BVP) by expanding the scattered acoustic pressure field into a series of point sources distributed on a fictitious surface placed inside the actual scatterer. This work provides additional code validation studies and illustrates the range of code parameters that produce accurate results with minimal computational costs. Systematic noise prediction studies are presented in which monopole generated incident sound is scattered by simple geometric shapes – spheres (acoustically hard and soft surfaces), oblate spheroids, flat disk, and flat plates with various edge topologies. Comparisons between FSC simulations and analytical results and experimental data are presented.

15. SUBJECT TERMS

acoustic scattering, benchmark scattering problems, fast scattering code

16. SECURITY CLASSIFICATION OF:			17. LIMITATION OF ABSTRACT	18. NUMBER OF PAGES	19a. NAME OF RESPONSIBLE PERSON
a. REPORT	b. ABSTRACT	c. THIS PAGE			STI Help Desk (email: help@sti.nasa.gov)
					19b. TELEPHONE NUMBER *(Include area code)*
U	U	U	UU	48	(443) 757-5802